STUDY OF PUPIL TRACKING SYSTEM TO IMPROVE OPTICAL COHERENCE TOMOGRAPHY PERFORMANCE FOR RETINAL DIAGNOSTICS

THANAPOL TUNTRAKUL

A Thesis Submitted in Partial Fulfillment of the Requirements for the
Degree of Doctor of Philosophy in Applied Physics
Suranaree University of Technology
Academic Year 2023

การศึกษาระบบติดตามรูม่านตาเพื่อปรับปรุงประสิทธิภาพของเทคนิคออพติกคอลโคเฮียเรนซ์โทโมกราฟฟีสำหรับการวินิจฉัยจอประสาทตา

นายธนพล ตันตระกูล

วิทยานิพนธ์นี้เป็นส่วนหนึ่งของการศึกษาตามหลักสูตรปริญญาวิทยาศาสตรดุษฎีบัณฑิต
สาขาวิชาฟิสิกส์ประยุกต์
มหาวิทยาลัยเทคโนโลยีสุรนารี
ปีการศึกษา 2566

STUDY OF PUPIL TRACKING SYSTEM TO IMPROVE
OPTICAL COHERENCE TOMOGRAPHY PERFORMANCE
FOR RETINAL DIAGNOSTICS

Suranaree University of Technology has approved this thesis submitted in partial fulfillment of the requirements for the degree of Doctor of Philosophy.

Thesis Examining Committee

(Asst. Prof. Dr. Chalongrat Daengngam)
Chairperson

(Assoc. Prof. Dr. Panomsak Meemon)
Member (Thesis Advisor)

(Prof. Dr. Joewono Widjaja)
Member

(Dr. Ittipon Fongkaew)
Member

(Dr. Wiwat Nuansing)
Member

(Assoc. Prof. Dr. Yupaporn Ruksakulpiwat)
Vice Rector for Academic Affairs
and Quality Assurance

(Prof. Dr. Santi Maensiri)
Dean of Institute of Science

ธนพล ตันตระกูล : การศึกษาระบบติดตามรูม่านตาเพื่อปรับปรุงประสิทธิภาพของเทคนิคออพติกคอลโคเฮียเรนซ์โทโมกราฟฟีสำหรับการวินิจฉัยจอประสาทตา (STUDY OF PUPIL TRACKING SYSTEM TO IMPROVE OPTICAL COHERENCE TOMOGRAPHY PERFORMANCE FOR RETINAL DIAGNOSTICS) อาจารย์ที่ปรึกษา : รองศาสตราจารย์ ดร. พนมศักดิ์ มีมนต์, 77 หน้า.

คำสำคัญ: การถ่ายภาพตัดขวาง, การถ่ายภาพจอประสาทตา, การติดตามรูม่านตา, ประสิทธิภาพการถ่ายภาพ

ประสิทธิภาพของการถ่ายภาพจอประสาทตาด้วยเทคนิคออพติกคอลโคเฮียเรนซ์โทโมกราฟฟี (Optical Coherence Tomography) หรือ โอซีที (OCT) เช่น ความละเอียดของภาพถ่ายและความลึกที่สามารถถ่ายได้นั้น มีความไวต่อการเคลื่อนไหวของดวงตาในขณะถ่ายภาพ และการวางตำแหน่งระหว่างเลเซอร์และรูม่านตา ดังนั้น เทคโนโลยีติดตามรูม่านตา (Pupil tracking) จึงเป็นส่วนสำคัญในการเพิ่มประสิทธิภาพของการถ่ายภาพจอประสาทตา ในปัจจุบัน เทคโนโลยีติดตามรูม่านตาที่ใช้สำหรับแอพพลิเคชันความเป็นจริงเสมือน (VR/AR) มีความน่าสนใจ เนื่องจากสามารถทำงานได้แม้ในสภาพแวดล้อมที่มีแสงรบกวนมาก ในส่วนของงานวิจัยนี้ จะเป็นการตรวจสอบการทำงานร่วมกันของระบบติดตามรูม่านตาที่ใช้สำหรับแอพพลิเคชัน VR/AR และระบบถ่ายภาพจอประสาทตาที่สร้างขึ้นเอง เรามีการวัดและเปรียบเทียบประสิทธิภาพของอัลกอริทึมติดตามรูม่านตาต่าง ๆ เพื่อที่จะหาอัลกอริทึมที่ดีและเหมาะสมสำหรับเครื่องถ่ายจอประสาทตาของเรา นอกเหนือจากนั้น ยังได้ศึกษาผลกระทบที่เกิดขึ้นต่อคุณภาพของภาพถ่ายจอประสาทตาด้วย

สาขาวิชาฟิสิกส์ ลายมือชื่อนักศึกษา ธนพล ตันตระกูล

ปีการศึกษา 2566 ลายมือชื่ออาจารย์ที่ปรึกษา

THANAPOL TUNTRAKUL : STUDY OF PUPIL TRACKING SYSTEM TO IMPROVE OPTICAL COHERENCE TOMOGRAPHY PERFORMANCE FOR RETINAL DIAGNOSTICS. THESIS ADVISOR : ASSOC. PROF. PANOMSAK MEEMON, Ph.D. 77 PP.

Keyword: Optical Coherence Tomography, Retinal imaging, Pupil tracking

The performance of Optical Coherence Tomography (OCT) retinal imaging, e.g., resolution, contrast, and depth penetration, is highly sensitive to eye motion and optical alignment between the eye's pupil and the laser beam. So, pupil tracking technology is very important to increase the performance of OCT retina imaging. The pupil-tracking technologies of AR/VR applications are interesting because they can work even in an open-field environment that has many strong light reflections. In this research, we aim to investigate the integration of the pupil-tracking technologies of AR/VR applications into our custom-designed pupil imaging system and OCT retinal imaging. The performances of each tracking technique in our pupil tracking system were measured and compared. Furthermore, their impacts on OCT retina image quality were studied.

School of Physics
Academic Year 2023

Student's Signature ธนพล ตันตระกูล
Advisor's Signature

ACKNOWLEDGEMENTS

I would like to thank my advisor, Assoc. Prof. Dr. Panomsak Meemon for providing me with the golden opportunity to conduct this research, as well as for his kind support and guidance, which was instrumental in the successful completion of my research. This research has significantly broadened my knowledge about optical and retinal imaging using optical coherence tomography.

I am grateful to Dr. Sorawis Sangtawesin and Dr. Ittipon Fongkaew for their valuable advice on programming. I also wish to extend my thanks to all the members of our research group for their help, suggestions, and friendship. My appreciation goes out to all the teachers who have imparted not only textbook knowledge but also life lessons to me.

I would like to thank my research examining committee, including Prof. Dr. Joewono Widjaja, Dr. Wiwat Nuansing, and Asst. Prof. Dr. Chalongrat Daengngam, for their insightful suggestions. I am thankful to the Development and Promotion of Science and Technology Talents Project for awarding me a scholarship.

Lastly, I wish to express my deepest appreciation and gratitude to my parents and family for their unwavering support, advice, understanding, encouragement, and love.

Thanapol Tuntrakul

CONTENTS

CONTENTS (Continued)

Page

CONTENTS (Continued)

LIST OF FIGURES

LIST OF FIGURES (Continued)

Figure **Page**

LIST OF FIGURES (Continued)

LIST OF FIGURES (Continued)

LIST OF FIGURES (Continued)

LIST OF FIGURES (Continued)

LIST OF FIGURES (Continued)

Figure **Page**

LIST OF FIGURES (Continued)

LIST OF FIGURES (Continued)

LIST OF ABBREVIATIONS

CT-scan	Computed Tomography scan
OCT	Optical Coherence Tomography
SUT	Suranaree University of Technology
TD-OCT	Time-Domain Optical Coherence Tomography
FD-OCT	Fourier-Domain Optical Coherence Tomography
SLD	Superluminescent Diode
FWHM	Full Width at Half Maximum
PSF	Point Spread Function
ExCuSe	Exclusive Curve Selector
ElSe	Ellipse Selector
PuRe	Pupil Reconstructor
PuReST	Pupil Reconstructor with Subsequent Tracking
Blob	Binary large object
mTCI	maximum Tissue Contrast Index
DC	Dispersion Compensator
OPL	Optical Path Length
FOV	Field of View
IR	Infrared
SD	Standard Deviation

CHAPTER I

INTRODUCTION

1.1 Background of study

Retinal disorders cover a wide range of conditions affecting the light-sensitive tissue at the back of the eye. They have diverse causes, symptoms, and effects on vision. For instance, Age-Related Macular Degeneration (AMD) is a progressive condition primarily affecting older adults, leading to central vision deterioration, blurred vision, and difficulty with tasks like reading and recognizing faces. Diabetic Retinopathy (DR) is a complication of diabetes that damages retinal blood vessels, potentially causing vision loss and even blindness. Retinal detachment occurs when the retina separates from its normal position, presenting symptoms like flashes of light, floaters, and a shadow in the visual field. Retinitis Pigmentosa (RP) is an inherited disorder causing night blindness and gradual peripheral vision loss. Macular Dystrophies affect the macula, leading to central vision loss and typically appearing in childhood or adolescence. Retinoblastoma is a rare eye cancer primarily affecting young children, potentially resulting in vision loss or life-threatening complications if not promptly treated (Ryan et al., 2012).

X-ray imaging has been widely used for diagnosing bone tissue abnormalities and certain medical conditions in the human body. However, its radioactivity poses a significant limitation as it can cause ionization of soft tissues, making it unsuitable for delicate structures like the eye's retina. To overcome these challenges, Computed Tomography (CT) scan was developed, a sophisticated imaging technique that combines X-ray images from various angles to create detailed 3D images with higher resolution. While CT-scan offers better anatomical assessment, it comes with drawbacks, including higher radiation exposure and increased cost and complexity. Both X-ray and CT-scan techniques are not suitable for in vivo retinal imaging due to

their potential radiation hazards and limited ability to capture fine retinal details (Fouras et al., 2009). Ultrasound is a high-frequency sound wave that finds application in soft tissue imaging, known as Ultrasound imaging, capable of producing 2D and 3D images. The advantage of Ultrasound lies in its non-radiation nature, eliminating the risk associated with X-ray and CT-scan. However, Ultrasound imaging has its limitations, primarily in terms of resolution, which is in the range of hundreds of millimeters to centimeters. Unfortunately, this resolution is inadequate for detailed retina diagnostics (Fouras et al., 2009).

Hermann von Helmholtz made a groundbreaking contribution to ophthalmology in 1851 with the invention of the first direct ophthalmoscope, depicted in **Figure 1.1**. This innovative device allowed for the examination of the interior of the human eye. The direct ophthalmoscope employs a semi-reflecting mirror to illuminate the eye with light. When both the patient's and the observer's pupils are optically aligned with the light source, as illustrated in **Figure 1.2**, the observer can visualize the patient's retina.

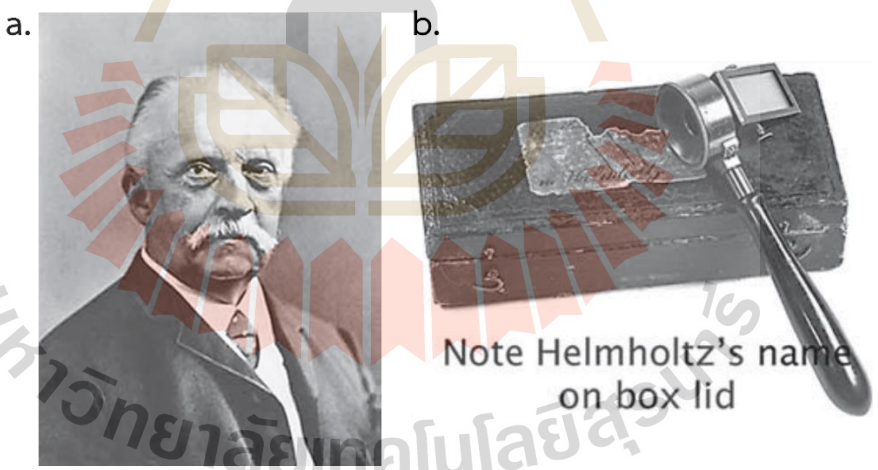

Figure 1.1 Hermann von Helmholtz (a.) and his ophthalmoscope (b.) (Pearce, 2009).

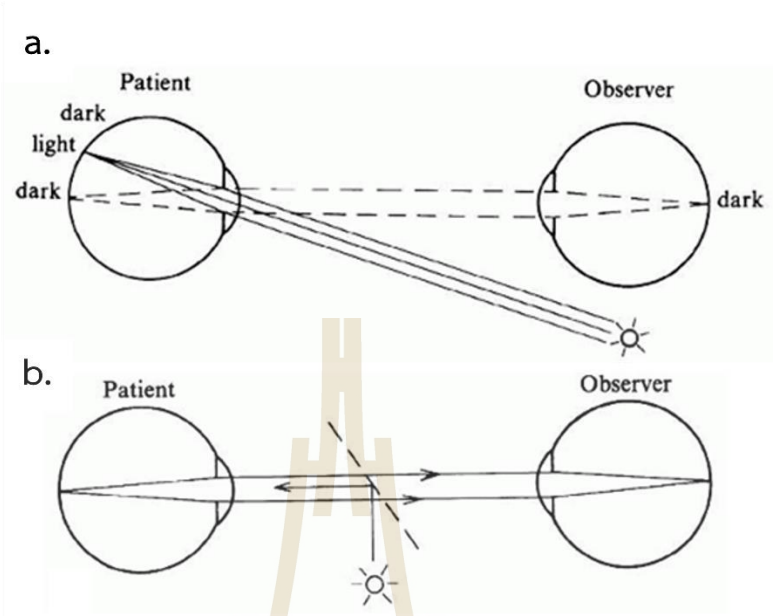

Figure 1.2 Direct ophthalmoscopy. (a.) If the light and observer are not aligned optically, the observer will not see the fundus that is illuminated. (b.) the light and the pupil of both patient and observer are aligned optically (https://entokey.com/principles-of-ophthalmoscopy/#R10-V1-63).

Despite its groundbreaking nature, the direct ophthalmoscope comes with limitations, including a restricted field of view of the back of the eye, and requiring the viewer to be in close proximity to the patient's face. To address these issues, Christian Georg Theodor Ruete introduced the first indirect ophthalmoscope in 1852, depicted in **Figure 1.3**. This innovative device allowed viewers to observe a wider field of view of the back of the eye, eliminating the need to stay close to the patient's face (Pearce, 2009). To achieve this expanded field of view, a lens was utilized instead of a mirror, positioned between the patient and the observer, as illustrated in **Figure 1.4**.

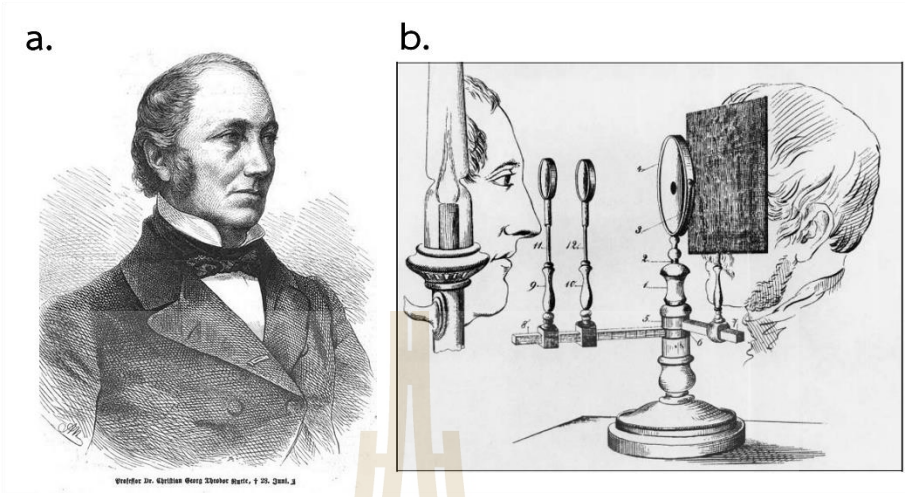

Figure 1.3 Christian Georg Theodor Ruete (a.) and the first indirect ophthalmoscope (b.) (Keeler, 2002), (https://de.wikipedia.org/wiki/Christian_Georg_Theodor_Ruete).

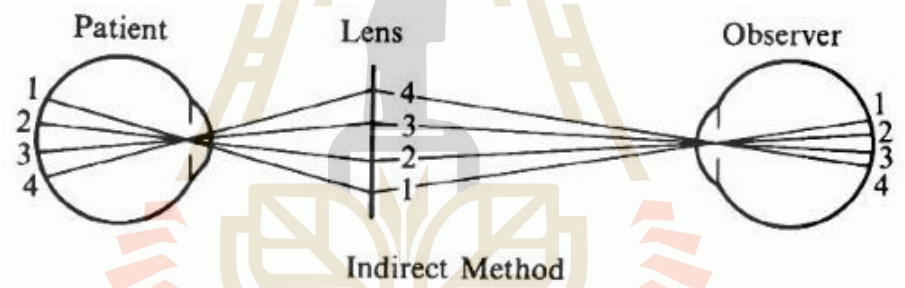

Figure 1.4 Indirect ophthalmoscope schematics (https://entokey.com/principles-of-ophthalmoscopy/#R10-V1-63).

However, it's important to note that both direct and indirect ophthalmoscopes are limited to capturing only the surface of the retina in a two-dimensional manner. Additionally, the accuracy of diagnosing retina disorders using these tools heavily depends on the expertise of the medical practitioner.

In 1961, Harold Novotny and David Alvis produced the first fluorescein angiogram as shown in **Figure 1.5**. It uses a fluorescent dye to be injected into the bloodstream. The dye can highlight the blood vessels in the back of the eye. So, the fluorescein angiogram can be used to help the doctor to diagnose eye disorders, such as macular degeneration and diabetic retinopathy. However, the fluorescein angiogram cannot image the sample in depth direction. Moreover, the fluorescein angiogram

requires injection of some chemical contents into the fundus which could introduce allergy and side-effect (Novotny and Alvis, 1961).

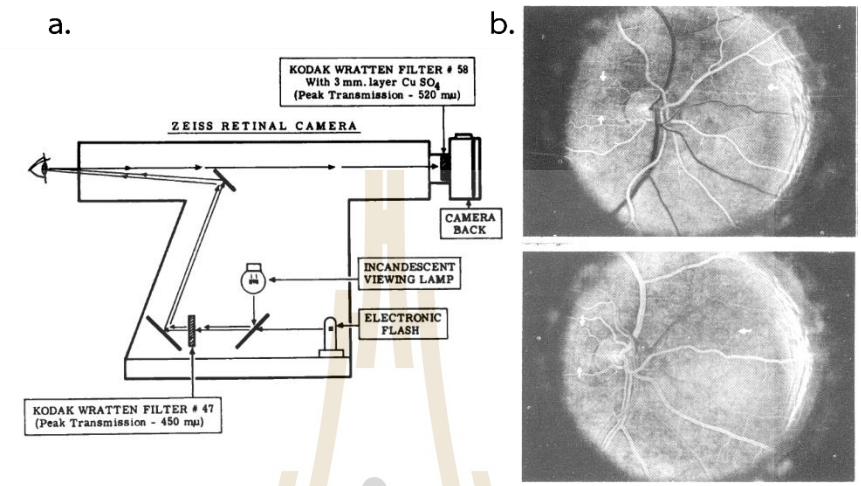

Figure 1.5 Cross-section of optical system of Zeiss fundus camera with filters inserted (a.) and the photograph from the first angiogram by Novotny and Alvis (b.) (Novotny and Alvis, 1961).

Nowadays laser technology has caused extensive optical imaging technology, which reduces patient exposure to harmful radiation by using visible and near infrared light. It is useful for soft tissues imaging. In addition, the speed and resolution of image obtained by optical instruments are much higher than those of Ultrasound.

For example, confocal microscope is used to analyze a structure of specific area within the cell. It uses laser to generate a high intensity of fluorescence and uses pinhole to eliminate out-of-focus signal as shown in **Figure 1.6**. It mainly uses with an anterior segment of the human eye such as the cornea (Organisciak and Vaughan, 2010). In addition, multiphoton microscope uses multiple infrared photons to excite the molecule then the molecule absorbs the photons and emits the fluorescence light as shown in **Figure 1.7** (Gibson et al., 2011). Multiphoton microscope is used for corneal imaging to diagnose a disease such as corneal dystrophies.

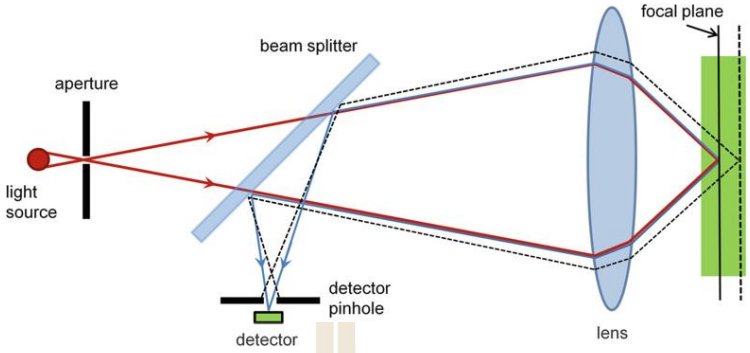

Figure 1.6 Confocal microscope scheme (Organisciak and Vaughan, 2010).

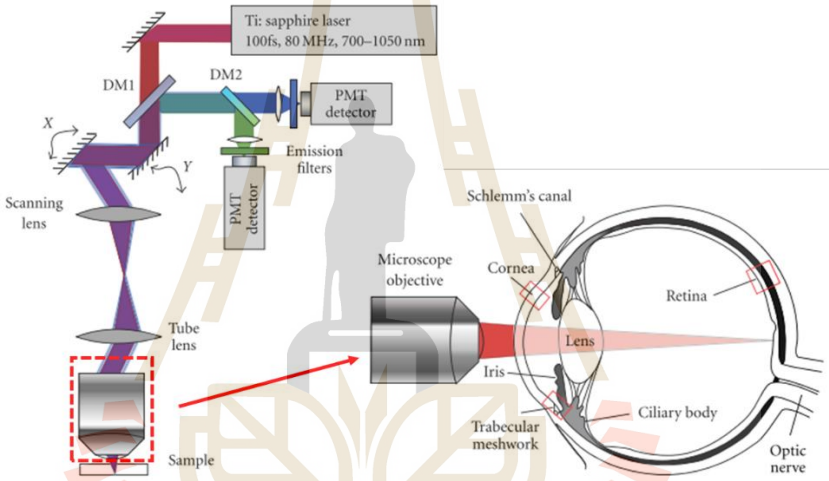

Figure 1.7 Schematic of a multiphoton imaging (Gibson et al., 2011).

Both confocal microscope and multiphoton microscope are suitable for studying cellular and subcellular level. They have a high resolution. However, they have low penetration depth, which is not sufficient for the entire thickness retina imaging.

In 1991, David Huang et al. developed the first optical coherence tomography (OCT) that is used for noninvasive and non-contact cross-section imaging of biological tissues. They used OCT to image the human retina and optic disk *in vitro* as shown in **Figure 1.8**. After that, the first *in vivo* measurements of human retinal structure with OCT were described by Eric A. Swanson et al. in 1993 as shown in **Figure 1.9**. Two years later, the first paper for the imaging of macular diseases with OCT was published by Carmen Puliafito et al. as shown in **Figure 1.10**.

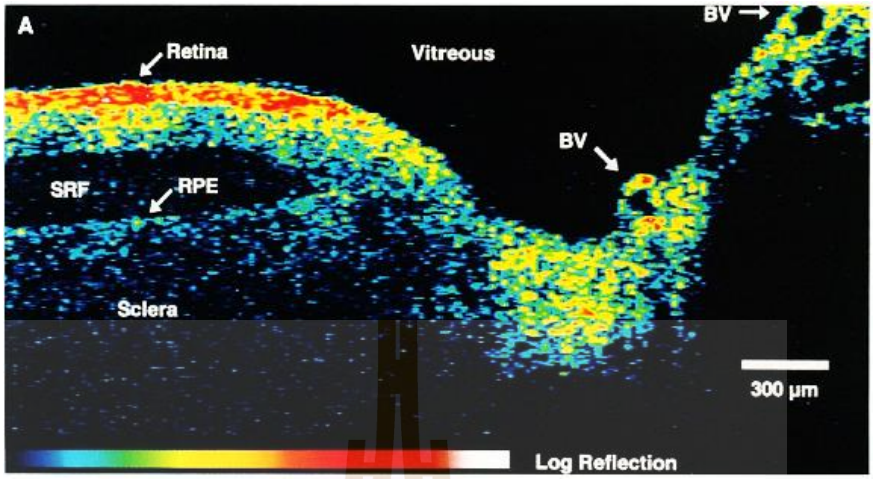

Figure 1.8 OCT of human retina and optic disk *in vitro* (Huang et al., 1991).

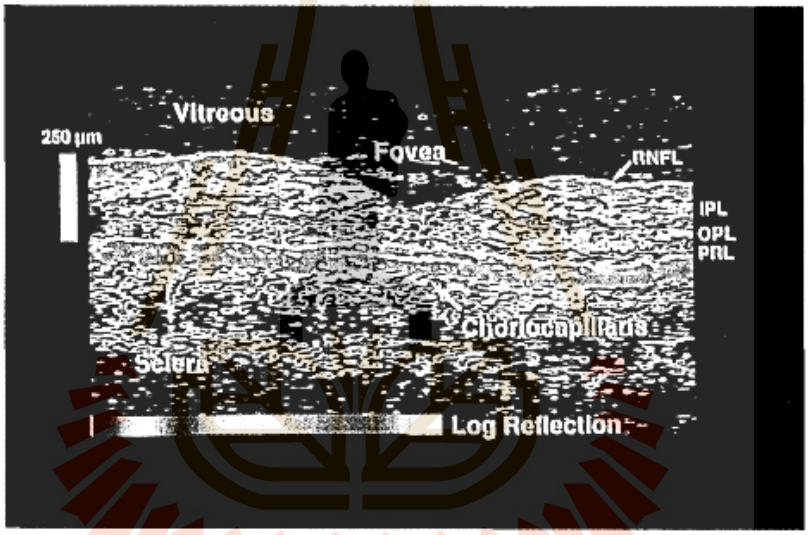

Figure 1.9 OCT of human retina in the macular region *in vivo* (Swanson et al., 1993).

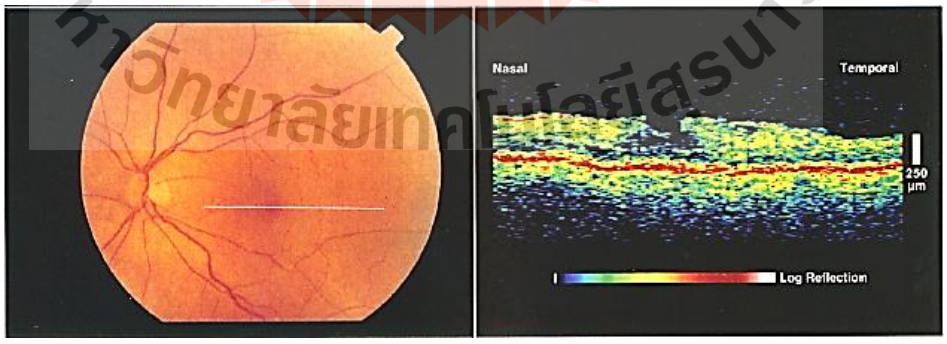

Figure 1.10 OCT image of a partial depletion of retinal tissue corresponding to the hole (Puliafito et al., 1995).

Since the first OCT is time-domain OCT (TD-OCT) as shown in **Figure 1.11** that uses the movement of the reference mirror for depth scanning of the sample, the speed of imaging is limited by the mechanical mirror scanning. To overcome the speed limit of TD-OCT, the new type of OCT was developed called: Fourier-domain OCT (FD-OCT) by Fercher in 1995 as shown in **Figure 1.12** (Fercher, Hitzenberger, Kamp, and El-Zaiat, 1995). FD-OCT does not require the scanning of a reference mirror, which enables it to get high-speed imaging. Maciej Wojtkowski et al. demonstrated the first *in vivo* tomograms of the human retina obtained by FD-OCT as shown in **Figure 1.13**. They were able to visualize details of the macular and optic disk *in vivo*.

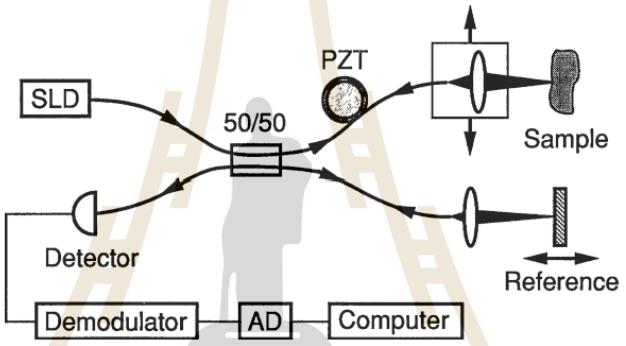

Figure 1.11 Time-domain OCT (Huang et al., 1991).

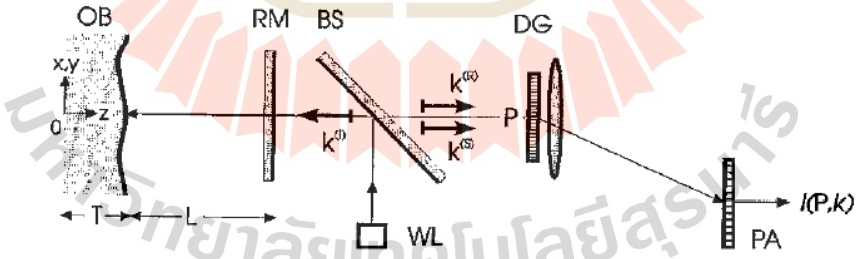

Figure 1.12 Fourier-domain OCT with "White" light source (WL). OB = object, RM = reference mirror, BS = beam splitter, DG = diffraction grating and PA = photodetector array (Fercher et al., 1995).

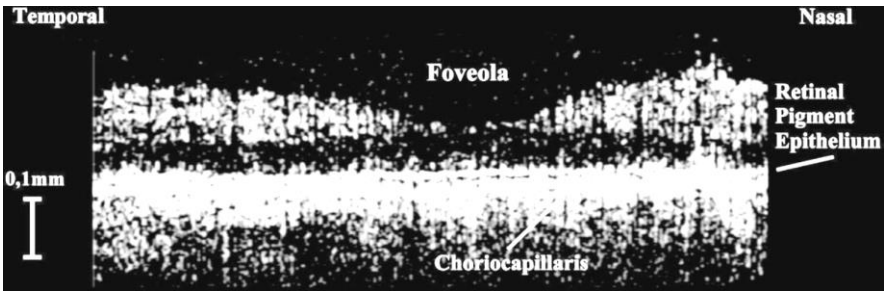

Figure 1.13 Tomogram of cross-section of the human retinal macula *in vivo* obtained by differential FD-OCT (Wojtkowski et al., 2002).

Due to the speed advantage of FD-OCT, we are interested in using this technique for the development of our OCT retina scanner prototype.

1.2 Significance of the study

OCT retinal imaging performance is highly influenced by factors such as eye motion, the alignment of the laser beam with the eye's pupil, and ambient room lighting, which influences pupil dilation. Achieving optimal image quality and signal-to-noise ratio requires careful management of these factors. In order to enhance the efficiency of collecting back-scattered light and minimize issues like aberrations and vignetting, it is common practice to align the scan pivot with the center of the ocular pupil (Carrasco-Zevallos et al., 2015). To accurately position the scan pivot, it is crucial to determine the precise location of the pupil. This process is referred to as pupil tracking, and it plays a vital role in shifting the scan pivot to the pupil for improved imaging outcomes.

Pupil tracking involves an image processing technique employed for real-time segmentation of pupil images and determining the center of the pupil. Two distinct types of pupil images exist: dark pupil and bright pupil images. The use of off-axis infrared (IR) light results in the appearance of a dark pupil image, while a bright pupil image is akin to the red-eye effect observed in flash photography. In scenarios where the IR illumination aligns directly with the pupil and the camera detects light reflected from the retina, a bright pupil image is generated (Morimoto et al., 2000). Bright pupil

images can exhibit variability due to factors like the angle of illumination, camera-to-eye distance, and other variables, posing challenges to achieving consistent and dependable tracking outcomes. Consequently, employing dark pupil images for tracking is considered more effective and efficient.

The Binary Large Object (Blob) detection algorithm, as described by Breuninger, Lange, and Bengler in 2011, is a widely used method for pupil tracking. It involves segmenting the pupil and determining its center. By employing this technique, the scanning beam can be precisely adjusted to the center of the pupil, thereby optimizing the optical power throughput of the imaging light beam, as highlighted by Carrasco-Zevallos et al. in 2015.

Tracking Scanning Laser Ophthalmoscope (SLO) is used for eye movement compensation. First, a fundus image (*En face*) is captured to be a reference frame. Then, each frame of B-scan is broken into strips and compared with the reference frame. If any strips are not match with the reference frame, the scanning plane is moved until the OCT image match with the reference frame (Sheehy et al., 2012; Vienola et al., 2012).

The difficulty to perform retina imaging does not only come from the eye motion but also bulk motion from head movement. Head movement decreases the pupil tracking accuracy as explained in (Zhu and Ji, 2005). They developed a pupil tracking algorithm that can solve this problem. However, the easy way to solve the head motion is head-mount eye tracking.

In present, head-mount eye tracking is constantly being developed to reduce the motion noise caused by the patient's head movement. The advantage of head-mount eye tracking is that it is compact and easy to carry and hence convenient to use outdoors. In addition, it can make pupil tracking easier as compared with the chin rest system because it does not consider the head movement.

Moreover, the conventional techniques of eye-tracking system in the commercial retinal OCT are mostly suitable for using in a dark room condition. For the open field environment, pupil tracking could be challenging because of strong light reflection on the pupil. Thus, new pupil tracking systems is demanded to solve this

problem (Fuhl et al., 2015). There are many methods of new pupil tracking systems that could work in the open environment, such as Swirski, Exclusive Curve Selector (ExCuSe), Ellipse Selector (ElSe), Pupil Reconstructor (PuRe), and Pupil Reconstructor with Subsequent Tracking (PuReST).

Though, all these tracking methods were compared in terms of detection rate and latency, they were mainly compared for AR/VR applications. To the best of our knowledge, their application and performance comparison for OCT retina imaging have not been yet studied and reported.

In our study, our objective is to explore the incorporation of various pupil tracking technologies into our pupil imaging system and OCT retinal imaging. We assessed and compared the performance of each tracking technique within our pupil tracking system. Additionally, we investigated their influence on the quality of OCT retina images and the speed of imaging.

1.3 Objectives

1) To design and build a laboratory prototype of an OCT retina scanner system.
2) To choose a pupil tracking algorithm that provides highest performance for the developed OCT retina scanner.

1.4 Scope of research

1) The OCT retina scanner was designed and built based on the principle of a spectrometer-based FD-OCT.
2) The operating light wavelength was around 880 nm with 45 nm optical bandwidth (INPHENIX SLD light source IPSDS0805).

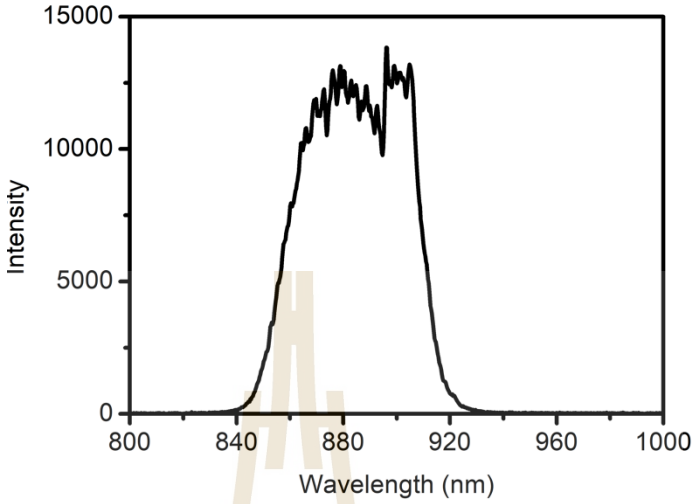

Figure 1.14 SLD broadband light source: central wavelength is about 880 nm, optical bandwidth is 45 nm, and the max power is about 6 mW (https:// www.inphenix.com/ en/broadband-light-source-modules/).

3) The detection unit was a commercially built high-speed spectrometer based on transmission grating from NIDEK RS300-OCT. A sensor is a linear CCD sensor (ATMEL AviiVA-SM2-CL) with 1024 resolution with 10 μm square pixels, and 53 kHz line rate.
4) The anterior segment of the eye model utilized a doublet lens (AC254-019-B-ML, Thorlabs, USA), while the posterior segment was sourced from Modell-Augen Manufaktur, Germany.
5) The pupil imaging system was designed and implemented on the OCT system.
6) Six pupil tracking algorithms, i.e., Blob detection, Swirski, ExCuSe, ElSe, PuRe, and PuReST, were implemented, and their tracking performances were compared.
7) The LabVIEW program was used for the OCT retina imaging.
8) The impact of each tracking algorithm on the OCT imaging was studied.

CHAPTER II

LITERATURE REVIEW

2.1 Optical Coherence Tomography (OCT)

2.1.1 Fourier-Domain OCT (FD-OCT)

OCT stands as a burgeoning optical imaging technique in the realm of biomedical optics and medicine. This innovative modality facilitates high-resolution, cross-sectional imaging of internal microstructures within biological tissues by capturing echoes of backscattered light. Employing interferometry, OCT achieves precise measurements of light echoes, utilizing three distinct interferometric detection techniques to gauge echo time delays.

In the initial stages, OCT instruments utilized a low-coherence light source and an interferometer featuring a scanning reference delay arm—a method known as low-coherence interferometry in the time domain. However, an alternative approach emerged, enabling detection in the Fourier domain by analyzing the interference spectrum. This groundbreaking concept, introduced by Fercher et al. more than a decade ago in 1995, marked a pivotal departure from traditional methodologies.

In 2003, three independent research groups demonstrated the formidable sensitivity advantage of Fourier domain detection over time domain detection. Fourier domain detection, by essentially measuring all light echoes simultaneously, ushered in a transformative era of heightened sensitivity in OCT research and development. This sensitivity enhancement, quantified by the ratio of axial resolution to axial imaging depth, translates into a substantial increase in imaging speeds—typically ranging from 50 to 100 times—in most OCT systems. This revelation has propelled OCT into the forefront of cutting-edge biomedical imaging technologies, promising unparalleled advancements in clinical diagnostics and research capabilities. (Drexler and Fujimoto, 2008)

2.1.2 Fundamental principle of FD-OCT

The schematic of low-coherence interferometer in FD-OCT can explain in **Figure 2.1**. The electric field of the low-coherence source can be expressed as

$$E_i(k) = E_0(k)e^{i(kz)}\,, \tag{2.1}$$

where k is the wave propagation number, E_0 is the electric field amplitude emitted by broadband light source, and z is the distance from the light source to the fiber coupler.

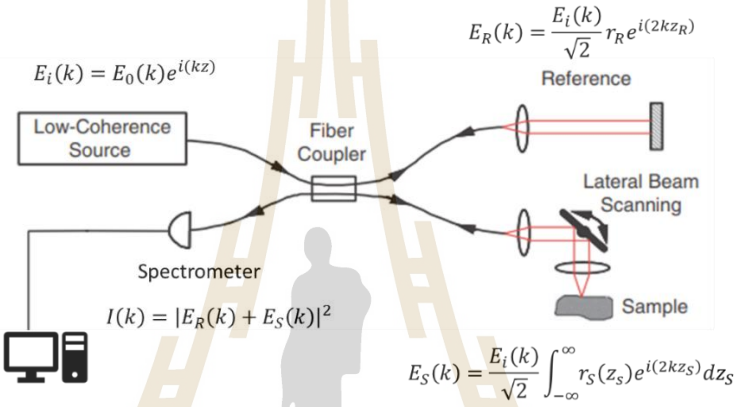

Figure 2.1 Schematic of low-coherence interferometry of FD-OCT (Adapted from (Drexler and Fujimoto, 2008)).

The electric field was split into two parts. The first part is reference arm which can be expressed by

$$E_R(k) = \frac{E_i(k)}{\sqrt{2}} r_R e^{i(2kz_R)}\,, \tag{2.2}$$

where r_R is the amplitude reflectivity of reference and z_R is the distance from the fiber coupler to the reference mirror. The second part is the sample arm. The electric field from the reflection and backscattered at the sample can be expressed as

$$E_S(k) = \frac{E_i(k)}{\sqrt{2}} \int_{-\infty}^{\infty} r_S(z_s) e^{i(2kz_S)} dz_S\,, \tag{2.3}$$

where $r_S(z_S)$ is the amplitude reflectivity of sample that depends on depth in sample and z_S is the distance from the fiber coupler to the sample. The interference between the electric field of the reference and sample arm was detected by the spectrometer. The intensity of the interference can be expressed as

$$I(k) = |E_R(k) + E_S(k)|^2\,, \tag{2.4}$$

$$I(k) = E_R(k)E_R^*(k) + E_S(k)E_S^*(k) + [E_R(k)E_S^*(k) + E_R^*(k)E_S(k)]\,, \quad (2.5)$$

where $E_R^*(k)$ and $E_S^*(k)$ are the complex conjugate of the electric field of the reference and the sample arm, respectively. There are three terms in Eq. (2.5). First, the DC term is the interference itself of the electric field at the reference arm ($E_R(k)E_R^*(k)$). Second, auto-correlation term (AC) is the interference itself of the electric field at the sample arm ($E_S(k)E_S^*(k)$). The last, cross-correlation term is the interference of the electric field between the reference and sample arm ($E_R(k)E_S^*(k) + E_R^*(k)E_S(k)$).

For the DC term, the intensity of DC term ($I_{DC}(k)$) can be reformulated by substituting Eq. (2.2) in the first term of Eq. (2.5),

$$I_{DC}(k) = \left(\frac{E_i(k)}{\sqrt{2}} r_R e^{i(2kz_R)}\right)\left(\frac{E_i(k)}{\sqrt{2}} r_R e^{-i(2kz_R)}\right), \quad (2.6)$$

$$I_{DC}(k) = S(k) r_R^2\,, \quad (2.7)$$

where $S(k)$ is the amplitude of the DC intensity, $S(k) = \frac{E_0^2(k)}{2}$.

For the AC term, the intensity of AC term ($I_{AC}(k)$) can be reformulated by substituting Eq. (2.3) in the second term of Eq. (2.5),

$$I_{AC}(k) = \left(\frac{E_i(k)}{\sqrt{2}} \int_{-\infty}^{\infty} r_S(z_s) e^{i(2kz_s)} dz_s\right)^2 \quad (2.8)$$

$$I_{AC}(k) = S(k)\left(\int_{-\infty}^{\infty} r_S(z_s) e^{i(2kz_s)} dz_s\right)^2 \quad (2.9)$$

For the cross-correlation term, the intensity of cross-correlation term ($I_{CC}(k)$) can be reformulated by substituting Eq. (2.2) and (2.3) in the third term of Eq. (2.5),

$$I_{CC}(k) = S(k) r_R \begin{bmatrix} e^{-i(2kz_R)} \int_{-\infty}^{\infty} r_S(z_s) e^{i(2kz_s)} dz_s \\ +e^{i(2kz_R)} \int_{-\infty}^{\infty} r_S(z_s) e^{-i(2kz_s)} dz_s \end{bmatrix}, \quad (2.10)$$

$$I_{CC}(k) = S(k) r_R \int_{-\infty}^{\infty} r_S(z_D)\left(e^{i(2kz_D)} + e^{-i(2kz_D)}\right) dz_D\,, \quad (2.11)$$

where z_D is the optical path difference between reference and sample arm,

$z_D = z_S - z_R$.

So, the interference intensity in the frequency domain can be expressed as

$$I(k) = I_{DC}(k) + I_{AC}(k) + I_{CC}(k)\,. \tag{2.12}$$

In practice, OCT signal is considered only the cross-correlation term. So, the interference signal is assumed to be $I(k) = I_{CC}(k)$ .The Fourier Transform equation is

$$\mathcal{F}\{f(x)\} = \int_{-\infty}^{\infty} f(x)e^{-ikx}dx\,, \tag{2.13}$$

so, $I_{CC}(k)$ can be reformulated to be

$$I(k) = I_{CC}(k) = S(k)r_R(\mathcal{F}\{r_S(-z_D)\} + \mathcal{F}\{r_S(z_D)\})\,. \tag{2.14}$$

To obtain the depth profile of the sample, the inverse Fourier Transform was used to the interference intensity. The Eq. (2.14) can be written as

$$\mathcal{F}^{-1}\{I(k)\} = \mathcal{F}^{-1}\{S(k)r_R\} * \left(\mathcal{F}^{-1}\{\mathcal{F}\{r_S(-z_D)\}\} + \mathcal{F}^{-1}\{\mathcal{F}\{r_S(z_D)\}\}\right)$$

$$I_{OCT}(z_D) = r_R\mathcal{F}^{-1}\{S(k)\} * \left(r_S(-z_D) + r_S(z_D)\right)\,. \tag{2.15}$$

From the **Figure 2.2**, the DC term appears at the zero position (the position has the same optical path as the reference arm). There are two peaks of the cross-correlation term. The first peak is the intensity of the surface at position z_{S1} . The second peak is the intensity of the surface at position z_{S2} .

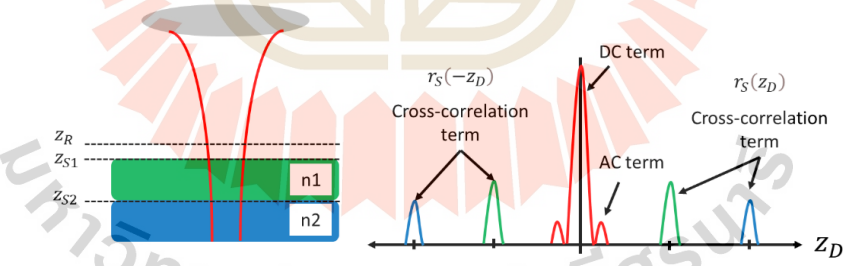

Figure 2.2 The depth profile of a sample that the OCT beam through at the different layer.

OCT system has two imaging resolutions. The first is the transverse resolution (Δx) which can be expressed as

$$\Delta x = \frac{4\lambda_0}{\pi}\frac{f}{D} \quad , \tag{2.16}$$

where λ_0 is the central wavelength of the low-coherence source, f is the focal length of the objective lens, and D is the diameter of the OCT beam. From the Eq. (2.16), the

transverse resolution in OCT is typically characterized as the focal diameter of the incident sample beam, and it remains unaffected by the coherence length of the light source (Wang and Wu, 2012). The second is the axial resolution (Δz) that can be expressed as

$$\Delta z = \frac{2ln(2)}{\pi}\frac{\lambda_0^2}{\Delta\lambda}, \tag{2.17}$$

where $\Delta\lambda$ is the Full-Width at Half Maximum (FWHM) of the low-coherence source.

2.1.3 Image formation

OCT achieves cross-sectional imaging by measuring the backscattered light's magnitude and echo time delay. This process involves conducting multiple axial measurements of echo time delay (referred to as axial scans or A-scans) while transversely scanning the incident optical beam, as illustrated in **Figure 2.3**. The outcome is a 2D dataset representing optical backscattering in a cross-sectional plane through the tissue. These datasets, known as B-scans, can be visually presented using false color or grayscale to highlight tissue pathology. For a more comprehensive representation of the tissue's structural information, three-dimensional (3D), volumetric datasets can be created. This is accomplished by acquiring sequential cross-sectional images through a raster pattern scan of the incident optical beam. 3D-OCT data provides extensive volumetric details, comparable to the manipulation of MR or CT images, opening up new possibilities for in-depth analysis and visualization (Drexler and Fujimoto, 2008).

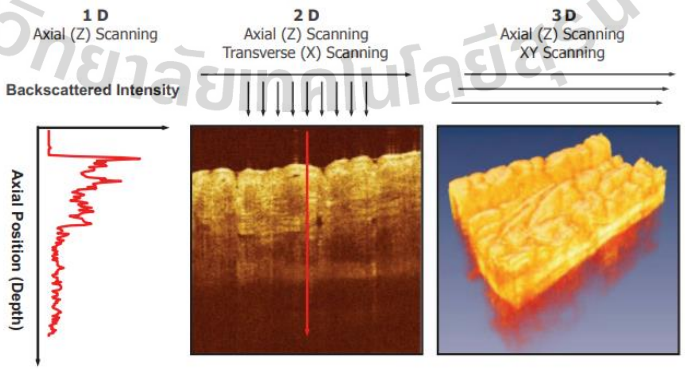

Figure 2.3 The processes to obtain the 1D, 2D, and 3D of OCT imaging (Drexler and Fujimoto, 2008).

2.2 OCT for retinal imaging and diagnostics

2.2.1 Optical system design of retinal OCT

The distinction in optical system design between standard OCT and retinal OCT lies in the sample arm as shown in **Figure 2.4**. In standard OCT, an objective lens is necessary to focus light onto the sample. In contrast, retinal OCT does not require an objective lens. Instead, it makes use of collimated light, which enters the pupil and is focused onto the retina by the eye's lens acting as the objective lens (Bille, 2019).

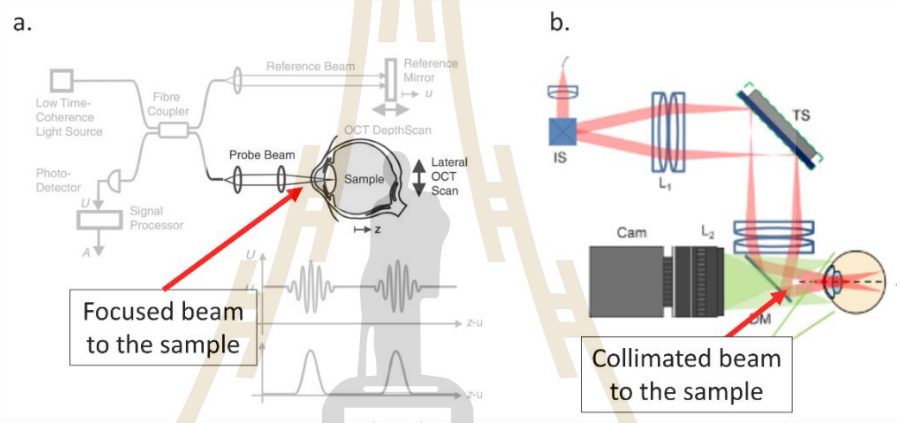

Figure 2.4 (a.) The standard OCT scans the sample by using the focused light (Adapted from (Bille, 2019)). (b.) The retinal OCT uses collimated light to incidence at the cornea. Then the eye's lens focuses light onto the retina (Adapted from (Carrasco-Zevallos et al., 2015)).

2.2.2 OCT for the retinal diagnostics

OCT has become a vital asset in retinal diagnostics, offering detailed and non-invasive imaging of retinal layers. Its significance is evident in the assessment of diabetic retinopathy, where OCT aids in detecting and monitoring diabetic macular edema, visualizing fluid accumulation in the macula to inform treatment decisions (Virgili et al., 2015). Additionally, OCT provides high-resolution imaging of the retinal nerve fiber layer, supporting the diagnosis and monitoring of conditions such as glaucoma, with changes in RNFL thickness indicating potential optic nerve damage (Oshitari et al., 2009). Furthermore, OCT angiography facilitates non-invasive imaging of retinal blood vessels, proving instrumental in diagnosing neovascular age-related

macular degeneration (AMD) and evaluating vascular changes in diabetic retinopathy (Waheed et al., 2016). In summary, OCT has transformed retinal diagnostics, offered detailed images and aiding in the diagnosis and management of diverse retinal conditions, making it an essential tool for eye care professionals.

2.2.3 Types of OCT for the retinal imaging

OCT for retinal imaging encompasses various types distinguished by the wavelength of the light source, a factor that significantly influences imaging depth and resolution. Time Domain OCT (TD-OCT), an early iteration, utilizes a low-coherence light source around 800 nm wavelength for detailed cross-sectional retinal imaging, providing axial resolution of 10 to 20 micrometers. However, its imaging speed is limited due to the mechanical movement of the reference arm mirror (Swanson et al., 1993). **Figure 1.9** showcases a retinal layer imaged using the TD-OCT technique.

Spectral Domain OCT (SD-OCT), also known as Fourier-Domain OCT, employs a broadband light source (840 nm to 870 nm) and a spectrometer to analyze backscattered light interference. SD-OCT offers substantial improvements in imaging speed, making it ideal for dynamic retinal imaging. It boasts higher axial resolution (5 to 7 micrometers), allowing detailed visualization of retinal layers and structures (Wojtkowski et al., 2002). **Figure 1.13** displays a retinal layer imaged through the SD-OCT technique.

Utilizing a rapidly tunable laser at approximately 1,050 nm wavelength, Swept-Source OCT (SS-OCT) enhances data acquisition speed compared to traditional SD-OCT. Notably, SS-OCT excels in depth penetration, particularly for imaging the choroid and retinal layers, as demonstrated in **Figure 2.5** ((Yasin Alibhai et al., 2018)). However, an inherent drawback of SS-OCT is its higher cost. The systems associated with SS-OCT are generally more expensive than those of SD-OCT due to the intricacy and expense of the rapidly tunable laser. This cost factor can pose a limitation, rendering SS-OCT a less economically viable option for certain clinical settings.

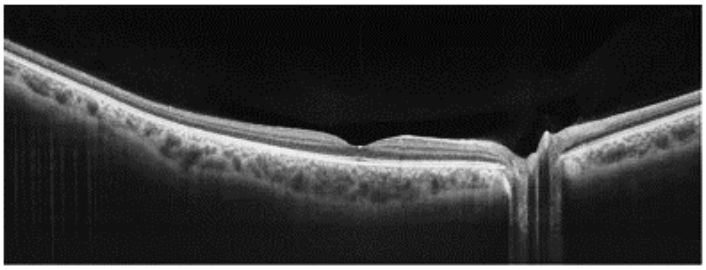

Figure 2.5 Normal retinal layer imaged with SS-OCT (Yasin Alibhai et al., 2018).

2.2.4 Advantages, disadvantages, and limitations of commercial OCT system in clinical ophthalmology

Commercially available OCT systems in clinical ophthalmology come with various advantages, disadvantages, and limitations. It's important to note that the specific characteristics can vary among different models and manufacturers as shown in Table 2.1 (Kiernan et al., 2010).

Table 2.1 Comparison of imaging speed and resolution between the commercial OCT.

Model name	Company name	A-scan per second	Axial resolution	Source wavelength
Cirrus HD-OCT	Carl Zeiss Meditec	27,000	5 μm	840 nm
Spectralis	Heidelberg Engineering, Vista, California, USA	40,000	7 μm	870 nm
RTVue-100	Optovue, Fremont, California, USA	26,000	5 μm	840 nm
3D-OCT 1000	Topcon, Paramus, New Jersey, USA	18,000	6 μm	840 nm
Spectral OCT and SLO	OPKO/OTI, Miami, Florida, USA	27,000	5 μm	-
SOCT Copernicus	Optopol, Zawiercie, Poland	25,000	6 μm	840 nm
Bioptigen SDOCT	Bioptigen, Durham, North Carolina, USA	20,000	4 μm	840 nm
Nidek RS-3000	Gamagori, Japan	53,000	7 μm	880 nm

2.2.5 Advancement & current technology of retinal OCT

While the OCT has successfully translated biophotonics science into clinical applications, its broader adoption beyond eye clinics faces constraints related to cost, size, and skill requirements. The existing generation of OCT systems, characterized by bulkiness, high expenses, and complexity, falls short of meeting the eye-care demands of the 6.5 billion individuals in low-income countries. Initiatives have been undertaken to overcome the limitations associated with OCT, and this includes the creation of affordable systems like SELF-OCT, designed to enable disease progression monitoring in the comfort of one's home (Chopra et al., 2021). Here are examples of the current technology of retinal OCT.

The Heidelberg Spectralis Flex Module as shown in **Figure 2.6**, a portable OCT device with a flexible arm extending up to 100 cm, facilitates adaptable positioning of the acquisition lens. This handheld device has been employed in diverse settings, including intensive care and surgery, offering comparable results to automated measurements from other OCT devices, such as central retinal thickness. However, the device is associated with a learning curve for operation and is still relatively heavy to hold or is attached to larger systems, limiting its use outside of the clinic (Chopra et al., 2021).

Figure 2.6 A portable OCT device with a flexible arm by the Heidelberg Spectralis Flex Module (Chopra et al., 2021).

To enhance accessibility and extend the utility of OCT into settings constrained by cost and size, developers have introduced portable, handheld devices as shown in **Figure 2.7**. These compact systems enable imaging of patients in various positions outside traditional outpatient clinics. Nonetheless, they come with limitations, including a steep learning curve for operation and susceptibility to motion artifacts (Chopra et al., 2021).

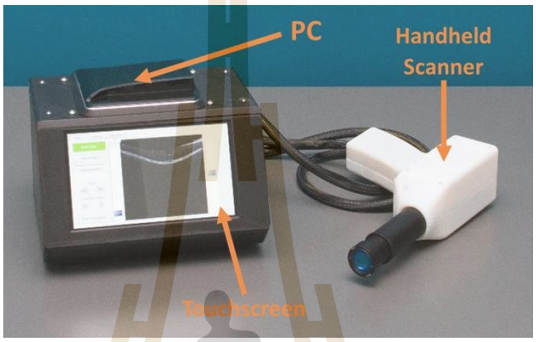

Figure 2.7 Low-cost, handheld OCT system created at Duke University (Chopra et al., 2021).

The MIMO-OCT system is an innovative home-based OCT system designed to produce single line scans or small volume scans with swift scanning capabilities and reduced density. Compact and portable, it enables OCT monitoring in the comfort of one's home. During the prototype phase, the subject's head was inclined downward onto the headrest to ensure stable positioning and minimize motion artifacts as shown in **Figure 2.8**. This cost-effective, portable OCT system holds promise in offering sufficient resolution for monitoring retinal diseases such as AMD, establishing itself as a practical choice for at-home OCT monitoring (Chopra et al., 2021).

Figure 2.8 MIMO-OCT system designed for home use.

2.2.6 Future trend of the retinal OCT

The design of a head-mounted OCT system prioritizes user comfort and ease of use during the testing process. Designed to be worn on the head, it allows for automatic alignment of the axial length with the selected target and guarantees appropriate lateral alignment so that the OCT light source can pass through the inspected eye's pupil. The device features a customizable frame, allowing for the analysis of both the left and right eyes, providing a thorough assessment as shown in **Figure 2.9**. Incorporated mechanisms for eye fixation, lateral, angular, and depth scanning of target regions contribute to heightened accuracy and versatility in measurements (Hogan, 2018).

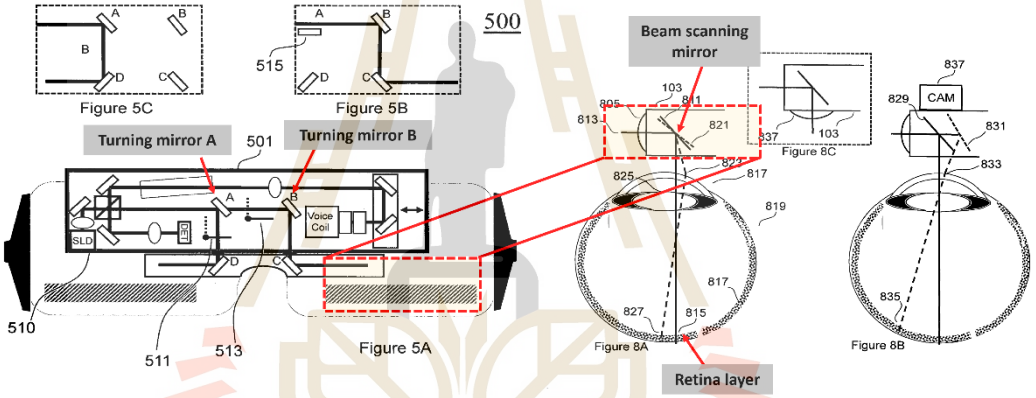

Figure 2.9 Head-mounted OCT design. To capture the retina of the left eye, the SLD light reflects off turning mirror A. On the other hand, to capture the retina of the right eye, turning mirror A is switched out of the path of the SLD light, allowing it to reflect off mirror B. Then the SLD light is scanned by beam steering mirror and go to the retina (Adapted from (Hogan, 2018)).

2.3 Conventional pupil tracking for OCT

In 2015, Heidelberg revolutionized ophthalmic imaging with a dual-beam system, reducing distortions from eye movements. This breakthrough enhanced OCT scan accuracy, enabling precise diagnosis and monitoring of eye conditions. Patented as TruTrack Active Eye Tracking, it became a standard in Heidelberg's OCT systems, setting a new industry benchmark for precision and efficiency in patient care as shown

in **Figure 2.10** (Mary Bramley, SPECTRALIS owner2015, <https://business-lounge.heidelbergengineering.com/gb/en/products/spectralis-spirit/spectralis-spirit/trutrack-active-eye-tracking/>).

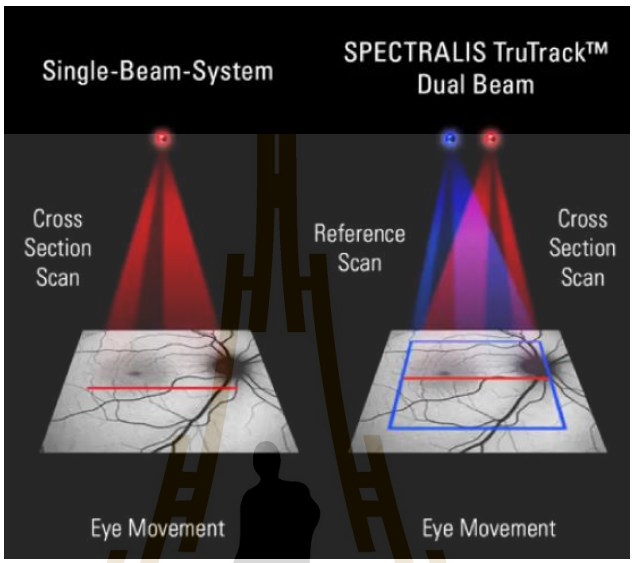

Figure 2.10 Eye movement compensation (TruTrack) by using a second beam (blue) to be a reference scanning. The reference scan will follow the eye movement. Then the cross-section scan (red) will follow the reference scan (https://www.youtube.com/watch?v=5r73QDir0U0).

In 2016, OPTOVUE advanced ophthalmic imaging technology significantly. They introduced an innovative method, combining a far camera with an XYZ stage for initial coarse adjustments to center and align the focal point in eye images. Following this initial alignment, OPTOVUE incorporated a near camera featuring a telecentric lens known for its shallow depth of focus. This specialized setup played a pivotal role in precisely determining the optimal focus for capturing detailed and crisp images of the eye. **Figure 2.11** vividly illustrates this groundbreaking process, offering a visual representation of OPTOVUE's ingenious methodology. The integrated use of far and near cameras, in conjunction with the XYZ stage, exemplifies a thorough and systematic approach to achieving unparalleled clarity and precision in ocular imaging (Wei et al., 2016).

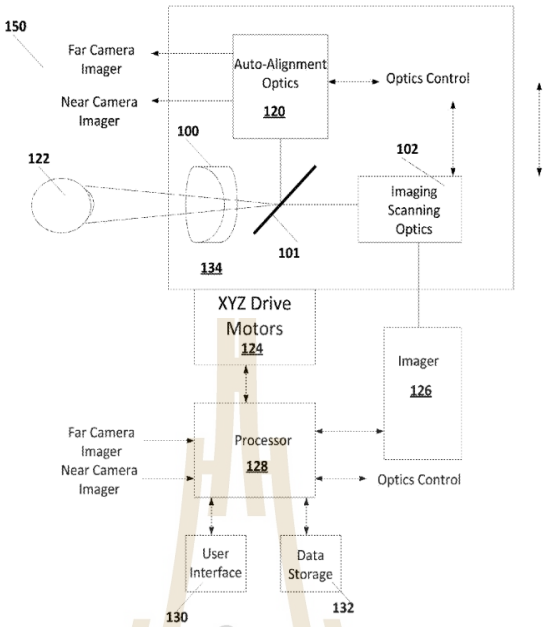

Figure 2.11 Schematic of the automatic optical alignment for OCT imaging (Wei et al., 2016).

In that very year, Topcon implemented a groundbreaking technique employing two anterior eye cameras for precise pupil alignment in both lateral (xy) and axial (z) directions, as illustrated in **Figure 2.12**. To ascertain the accurate position of the pupil, the images captured by both cameras must seamlessly align, exemplified in **Figure 2.13**. (Fukuma et al., 2016).

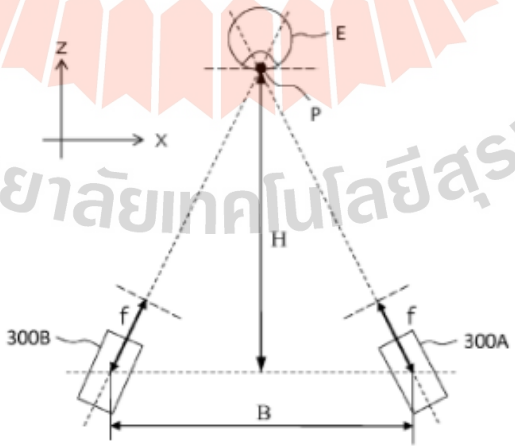

Figure 2.12 Schematic of pupil tracking by using two cameras (300A and 300B) at the different direction (Fukuma et al., 2016).

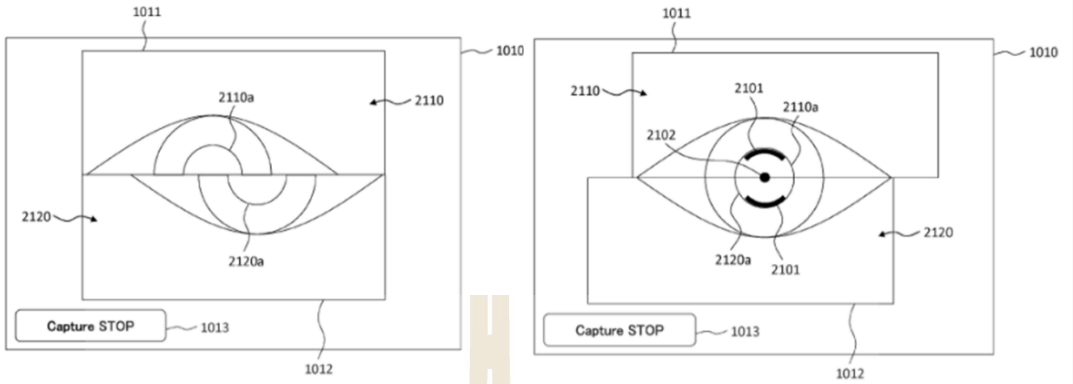

Figure 2.13 Screen display of pupil alignment. The half of two camera (300A and 300B in Figure 17) were display as 2110 and 2120, respectively (Fukuma et al., 2016).

2.4 Alternative pupil tracking algorithms for open field environments

The conventional pupil tracking of OCT commercials is usually used in a dark room condition. The pupil tracking in the open field environment is difficult because of a strong light reflection on the pupil. To increase the performance of pupil tracking in an open field environment, alternative pupil tracking algorithms were used to solve this problem. There are five algorithms that were used in this research.

Binary large object (Blob) detection in OpenCV can accurately estimate the pupil's area and pupil's center, which corresponds to the given parameters based on group of connected pixels as shown in **Figure 2.14** (Casas and Chandrasekaran, 2019). **Figure 2.15** show the pupil tracking by using Blob detection.

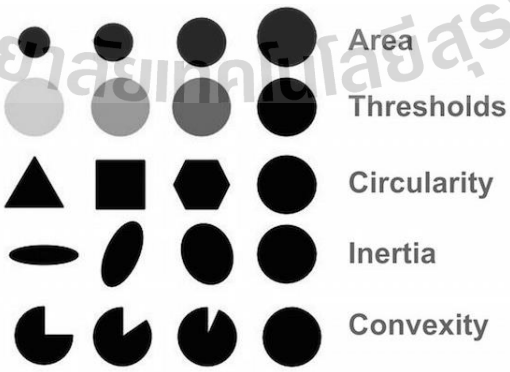

Figure 2.14 The parameters which are used to filter the type of blobs that we want to detect (https://learnopencv.com/blob-detection-using-opencv-python-c/).

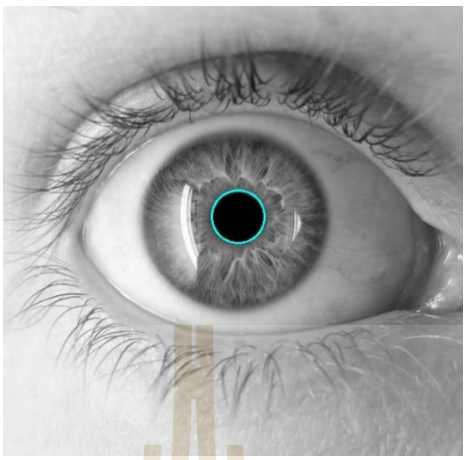

Figure 2.15 Pupil tracking by using Blob detection in OpenCV (https://craftofcoding.wordpress.com/2017/12/13/pupil-segmentation-with-blobs/).

Swirski technique uses the dark pupil tracking algorithm for the approximation of the pupil region to reduce the search space. A k-means histogram segmentation is used to find an elliptical pupil shape and the pupil's center. Finally, Random Sample Consensus (RANSAC) (Fischler and Bolles, 1981) is used for an ellipse fitting of a pupil as shown in **Figure 2.16** (Świrski et al., 2012).

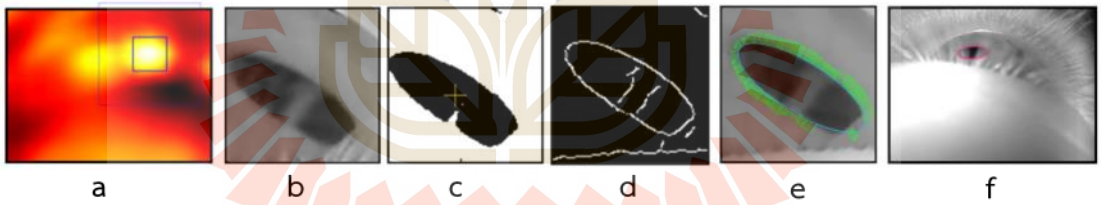

Figure 2.16 Pupil tracking steps of Swirski technique; (a.) Approximation of pupil region by Haar-like center surround feature. (b.) Pupil segmentation by k-means histogram and the darkest region is assumed to be a pupil (c.). (d.) Canny edge detection is used to find pupil's edge. Finally, ellipse fitting is estimated by RANSAC (e.) and the result of pupil tracking as shown in (f.) (Fuhl, Tonsen, et al., 2016).

Exclusive Curve Selector (ExCuSe) technique uses peak detection from the intensity histogram to analyze images. If the peak is detected, a pupil can be found based on edge filtering. If not, threshold the image and the Angular Integral Projection Function (AIPF) (Mohammed et al., 2010) will be used for the coarse positioning as shown in **Figure 2.17** (Fuhl et al., 2015).

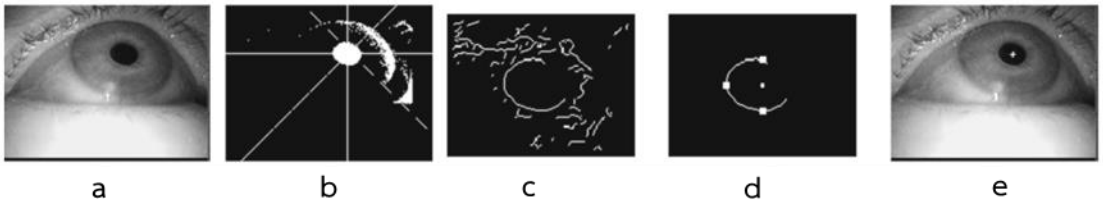

Figure 2.17 Pupil tracking steps of ExCuSe technique; (a.) Input image. (b.) The coarse positioning of pupil is approximated by AIPF. (c.) Canny edge detection is used to find pupil's edge. (d.) To find the pupil border, rays are sent out from the middle white point (the best estimation of the pupil's center) to all directions and the line intersection is pupil's edge. Finally, the pupil's center is calculated by the center of mass of ellipse (e.) (Fuhl, Tonsen, et al., 2016).

Ellipse Selector (ElSe) technique applies the Canny edge filter (Canny, 1986) to an eye image. Then the edges are manipulated by Morphologic patterns. Next, the least-squares ellipse fitting was used for ellipse fitting. The best ellipse to represent the pupil is chosen by the lowest inner gray value and the roundest shape. If this method fails, the convolution filter with the downscale image was used to find the coarse position of a pupil. Then the neighborhood of the coarse position was thresholded. The center of mass of the threshold pixel is the pupil center position as shown in **Figure 2.18** (Fuhl, Santini, et al., 2016).

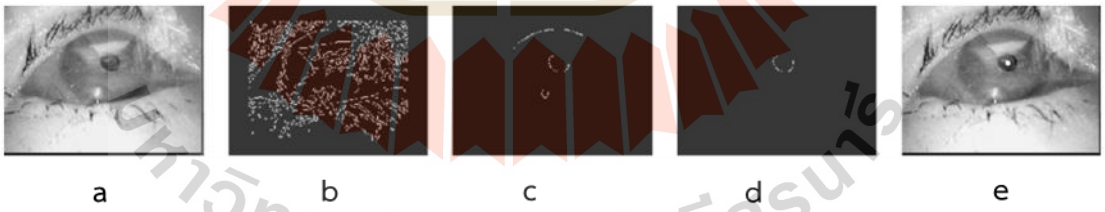

Figure 2.18 Pupil tracking steps of Else technique; (a.) Input image. (b.) Find pupil's edge by Canny edge filter. (c.) Edge filtering by curvature analysis. (d.) The lowest intensity of the best curvature is to be a pupil. (e.) The pupil's center is calculated by the center of mass (Fuhl, Tonsen, et al., 2016).

Pupil Reconstructor (PuRe) technique has two assumptions to constrain the dimension space of a pupil: 1) the eye canthus lay within an image, and 2) the eye canthus covers at least two-thirds of the image diagonal. The first is edge detection.

The Canny edge detection (Canny, 1986) is used to create an edge image. The edge image is manipulated with a morphological approach. The second is edge selection. The k-cosine chain approximation method was used to approximate each edge segment so that the ellipse fitting is better. Least-square ellipse fitting was employed for the final fitting process. Finally, the candidate of each ellipse fit is evaluated by the confidence measure to be a pupil (Santini et al., 2018a).

The Pupil Reconstructor with Subsequent Tracking (PuReST) technique uses the PuRe technique for initial pupil detection. Then the square region of interest (ROI) is created at the pupil's center of the previous frame. Within this ROI, there are two methods for pupil detection. First, an outline tracker is used to locate the pupil in the previous frame by evaluating between the pupil's outline and the pupil's ellipse fitting. The second, a greedy tracker is used to combine a good edge segmentation to reconstruct and detect the pupil for the subsequent frame (Santini et al., 2018b).

2.5 Measurement of pupil tracking performances

2.5.1 Pupil tracking accuracy

Detection rate is the pupil tracking performance that represents the tracking precision of an algorithm. It considers a pupil center detection at the difference pixel error based on the Euclidean distance between the ground-truth and each algorithm as shown in **Figure 2.19** (Fuhl et al., 2015).

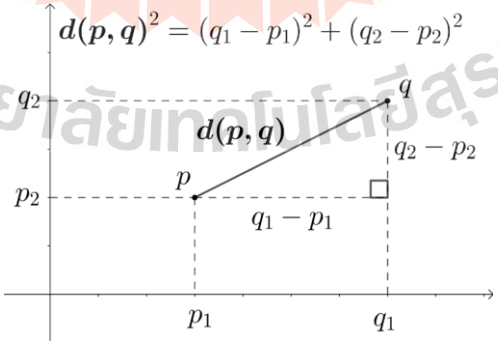

Figure 2.19 The Euclidean distance (d) between point (p) and (q) (https://en.wikipedia.org/wiki/Euclidean_distance).

There are many pupil tracking algorithms that use the detection rate to compare the tracking performance. In 2012, Swirski proposed a robust real-time pupil tracking in highly off-axis images (Świrski et al., 2012). Then to increase the detection rate, Exclusive Curve Selector (ExCuSe) was proposed in 2015 (Fuhl et al., 2015) as shown in **Figure 2.20**.

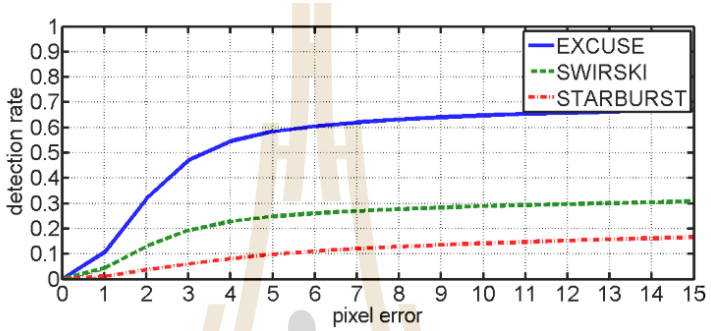

Figure 2.20 The detection rate between 3 algorithms, ExCuSe, Swirski, and Starburst (Fuhl et al., 2015).

Later, Ellipse Selector (ElSe) was proposed to increase detection rate 14.53% relative to the previous algorithms (Fuhl, Santini, et al., 2016). However, a processing time of ElSe is higher than Swirski and ExCuSe (Santini et al., 2018a). In 2018, Pupil Reconstructor (PuRe) was proposed to increase the detection rate and reduce a processing time compared with the ElSe (Santini et al., 2018a) as shown in **Figure 2.21**.

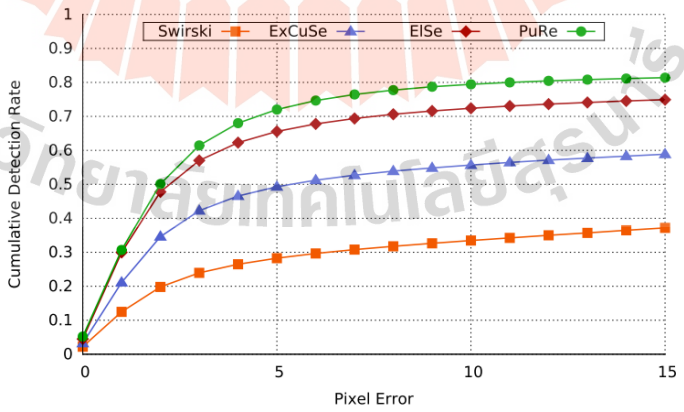

Figure 2.21 The detection rate comparison between four tracking algorithms (Santini et al., 2018a).

Nevertheless, the processing time of PuRe is still higher than the ExCuSe. In the same year, Pupil Reconstructor with Subsequent Tracking (PuReST) was proposed. Both detection rate and processing time of this algorithm are better than the previous algorithm (Santini et al., 2018b) as shown in **Figure 2.22**.

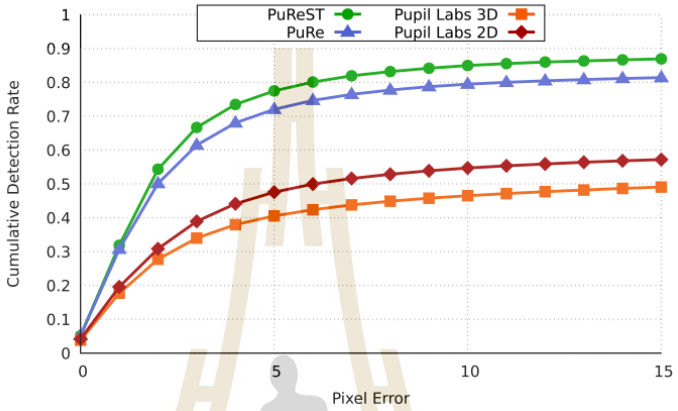

Figure 2.22 The detection rate between PuRe and PuReST (Santini et al., 2018b).

2.5.2 Pupil tracking speed and latency

Latency plays a crucial role in real-time pupil tracking, directly impacting the speed of the tracking process. It represents the duration between the image capture by the sensor and the pupil tracking output generated by the algorithm.

The latency or run-time measurements were evaluated for each algorithm, as depicted in **Figure 2.23**. In the top portion of **Figure 2.23**, the ExCuSe algorithm demonstrated the swiftest run time at 2.51 ms, followed by the Swirski algorithm at 3.77 ms, the PuRe algorithm at 5.56 ms, and the ElSe algorithm at 6.59 ms (Santini et al., 2018a). While ExCuSe exhibited the fastest run time, its detection rate was lower compared to PuRe. In order to enhance both, run time and detection rate, the PuReST algorithm was introduced. PuReST boasts a run time of approximately 1.88 ms, surpassing ExCuSe's run time (Santini et al., 2018b), as illustrated in the bottom portion of **Figure 2.23**.

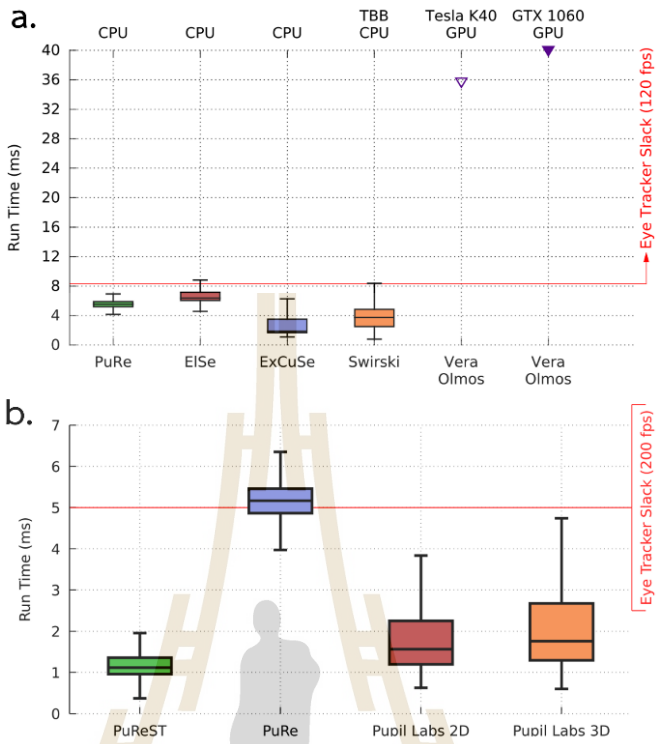

Figure 2.23 (a.) The latency or run time measurement between 4 algorithms (Swirski, ExCuSe, ElSe, and PuRe) (Santini et al., 2018a). (b.) The latency measurement of PuRe and PuReST (Santini et al., 2018b).

2.5.3 Assessment of signal quality on OCT retinal image

Signal quality assessment of retinal OCT images is a crucial step in the treatment of retinal diseases. The quality of OCT images can be affected by various factors such as motion artifacts, media opacities, and signal strength Accurate assessment of the signal quality of OCT images is essential for accurate segmentation, measurement, and quantification of retinal images. There are several methods to assess the signal quality of OCT retinal images, such as Manufacturer Signal Index (MSI) and the maximum Tissue Contrast Index (mTCI) (Huang et al., 2012).

Each retinal OCT device utilizes Manufacturer Signal Index (MSI) as a parameter to evaluate the signal quality of OCT images. Y. Huang et al. reported an assessment of four spectral domain OCT devices (Cirrus, RTVue, Spectralis, and 3D OCT-1000), with each device assigning an MSI value to the multi-frame OCT images. While Cirrus, RTVue, and 3D OCT-1000 assigned a single MSI value per multiframe image,

Spectralis assigned an MSI value per frame, subsequently calculating the average MSI for the multiframe image. Despite this, the varied units and values for MSI among different devices pose challenges in comparing signal quality. Additionally, MSI values are derived from the respective devices' review software, potentially lacking standardization and universal applicability.

As a result of overcoming the limitations of the MSI approach, the maximum Tissue Contrast Index (mTCI) is proposed. The assessment of signal quality in retinal OCT images involves a detailed analysis of the intensity levels of background and foreground pixels. This evaluation is measured by applying the mTCI, as outlined in Eq. (2.18) (Y. Huang et al., 2012), utilizing the intensity histogram of cross-section images, as depicted in **Figure 2.24**(a.) and (b.).

$$mTCI = \frac{(N_3 - N_1)}{(N_2 - N_1)}. \tag{2.18}$$

The computed $mTCI$ values for the OCT images shown in **Figure 2.24 (c.)** were determined to be 6.95, 5.55, and 3.50, respectively. These values serve as a quantitative measure of the contrast and clarity of the retinal OCT images, providing valuable insights into the overall signal quality and potential diagnostic utility of the captured data. This rigorous assessment ensures that the acquired OCT images are of the highest quality, enabling accurate interpretation and aiding in precise clinical decision-making.

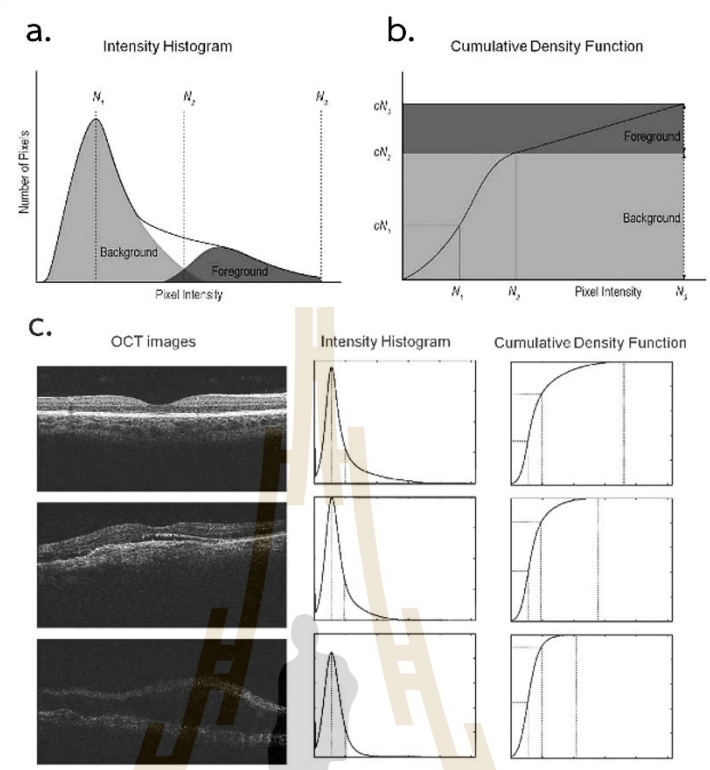

Figure 2.24 (a.) The intensity histogram of OCT image that shows the relative composition between background and foreground pixel. N_1, N_2, and N_3 are the signal intensity value at the separation point. (b.) The cumulative density function of OCT image. (c.) The comparison of intensity histogram and cumulative density function between three OCT images.

CHAPTER III

RESEARCH PROCEDURE

3.1 Design of the OCT retina scanner prototype

OCT retina imaging was based on Michelson interferometry as shown in **Figure 3.1**. First, the near-infrared broadband laser (INPHENIX SLD light source IPSDS0805) with wavelength 880 nm was used to be a light source. The laser source was collimated by the collimator providing a 4 mm beam diameter (CFS18-850-APC, Thorlabs, Inc.). Then the laser beam was split into two paths, i.e., sample path and reference path, by a 50/50 fiber beam splitter (TW850R5A1, Thorlabs, Inc.). The sample path includes both the OCT retina scanner and the pupil tracking system. The OCT retina scanner used galvanometers (Galvo) for beam scanning and two lenses for the relay system. The pupil-tracking system included a pupil-tracking camera and infrared illumination. More information about this component can be found in sections 3.2 and 3.3. For a reference path, the collimated beam passed through the dispersion compensator (DC: Water cube, 24 mm long, closed at the head and ended with a cover slide.) and reflected the reflection grating (GR25-1208, Thorlabs, Inc.). Then the laser was focused by achromatic doublet lens (AC254-100-B-ML, Thorlabs, Inc.) to the mirror (PF10-03-P01, Thorlabs, Inc.). DC and reflection grating were used to compensate the optical path length (OPL) and dispersion mismatch from both eye and optical lens in a sample path. The interference between the reflected light returned from a sample path and a reference path occurred in a fiber beam splitter and was transmitted to the detector via a fiber. After that, the interference signal was diffracted by a transmission grating in the detection part. Each wavelength from a diffraction was focused on the CCD camera sensor (ATMEL AViiVA-SM2-CL) by lens. The interference signal was obtained as a function of the wavelength of the light source. Finally, the interference signal was Fourier transformed to be a depth profile of the sample reflectivity. To obtain the

cross-section image, the XY galvo (GVS002, Thorlabs, Inc.) were used for lateral scanning of a sample light beam. All depth profiles were combined to be a depth cross-section image.

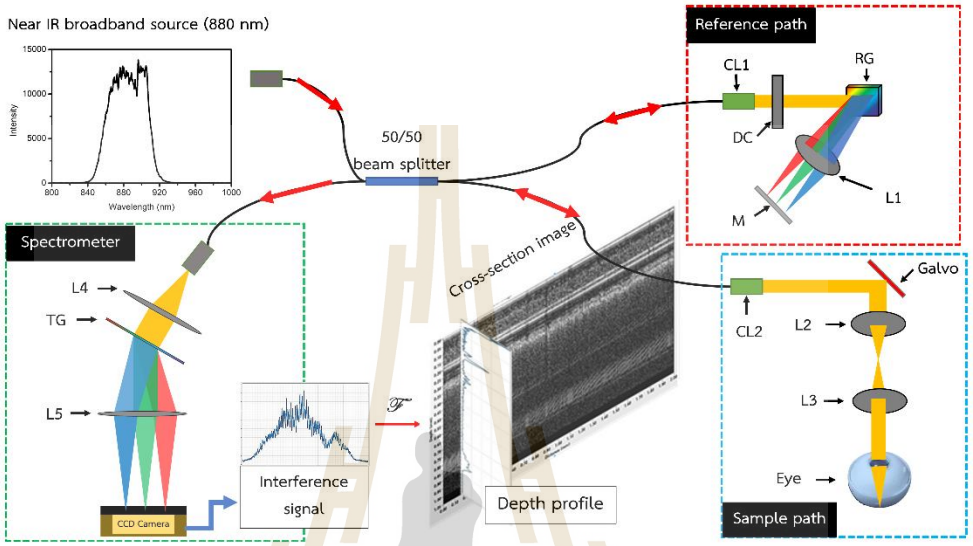

Figure 3.1 The OCT schematic for retina imaging involves the following steps: The near-infrared broadband was divided into a reference path and a sample path. The reflections of light from both paths converge at a beam splitter to create interference. The CCD camera sensor detects the interference signal. Ultimately, Fourier transformation is applied to convert the interference signal into the cross-sectional image of the retina.

The OCT retina scanner head was design and built in our laboratory as shown in **Figure 3.2**(a.). The XYZ stages were used for alignment between a laser beam and the patient's eye. To reduce the motion artifact from the patient's movement, a chin rest was implemented to the OCT retina scanner. There are two parts in the sample arm, consisting of the OCT retina scanner and the pupil tracking as shown in **Figure 3.2**(b.).

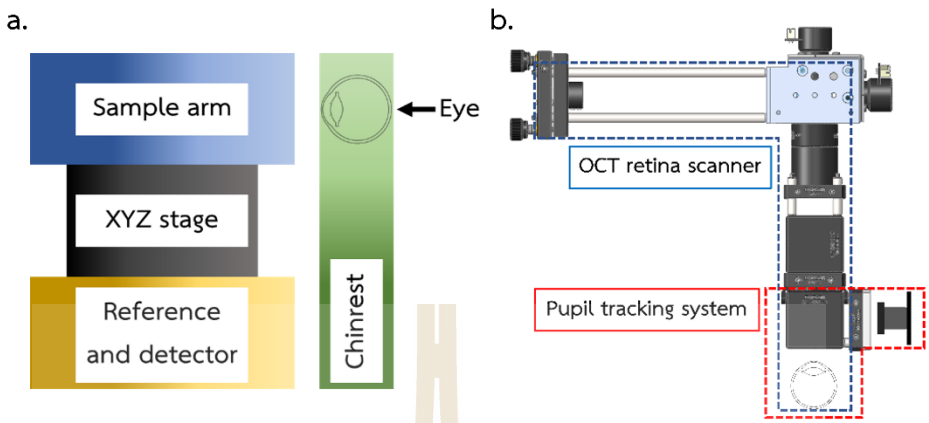

Figure 3.2 (a.) Design of the OCT retina scanner. (b.) Two components within the sample arm. The blue section represents the OCT retina scanner utilized for cross-sectional retina imaging. The red section denotes the pupil tracking system, employed for aligning the OCT beam with the pupil to enhance image quality.

3.2 Integration of OCT retina scanner and pupil tracking system

From the schematic of the sample arm in **Figure 3.3**, laser was collimated by the collimator (CFS18-850-APC, Thorlabs, Inc.). After that, laser reflected the galvo (GVS002, Thorlabs, Inc.), which was used for lateral beam scanning. Lens 1 (AC254-035-B-ML, Thorlabs, Inc.) and Lens 2 (AC254-050-B-ML, Thorlabs, Inc.) were used to relay the pivot point of the galvo to the pupil. Finally, the eye's lens served as an objective lens for focusing the OCT beam on the retina.

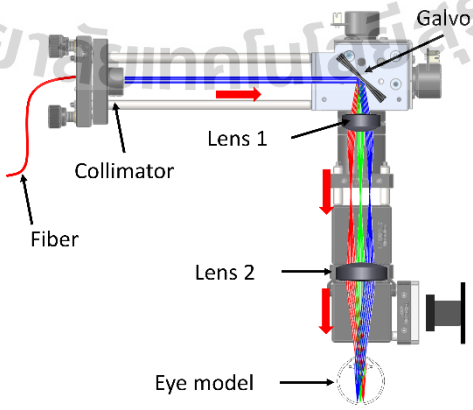

Figure 3.3 The schematic of the OCT retina scanner part.

3.3 Pupil tracking system

In the hardware setup, the implemented OCT retina scanner was equipped with 3-axis motorized translation stages. A tracking camera (USB digital camera module, 640x480 pixel resolution at 30 frame rate, 55° FOV) was used to capture an image of the eye to be used for pupil tracking. The camera part was combined with the OCT retina scanner as shown in **Figure 3.4**(a.). **Figure 3.4**(b.), the focal length was adjusted to the pupil (fixed at the focal length of Lens 2 in **Figure 3.3**) through the movement of the 3-axis motorized translation stages. To improve the pupil contrast, an off-axis IR illuminator (wavelength 940 nm **Figure 3.4**(c.)) was used to illuminate an eye as shown in **Figure 3.4**(a.). Dichroic mirror (DM1) with 900 nm cut off (DMSP900R, Thorlabs, Inc.) was used to reflect the IR illumination from a pupil to the camera. The intensity of OCT beam (wavelength 880 nm) was maintained after double pass through a DM1.

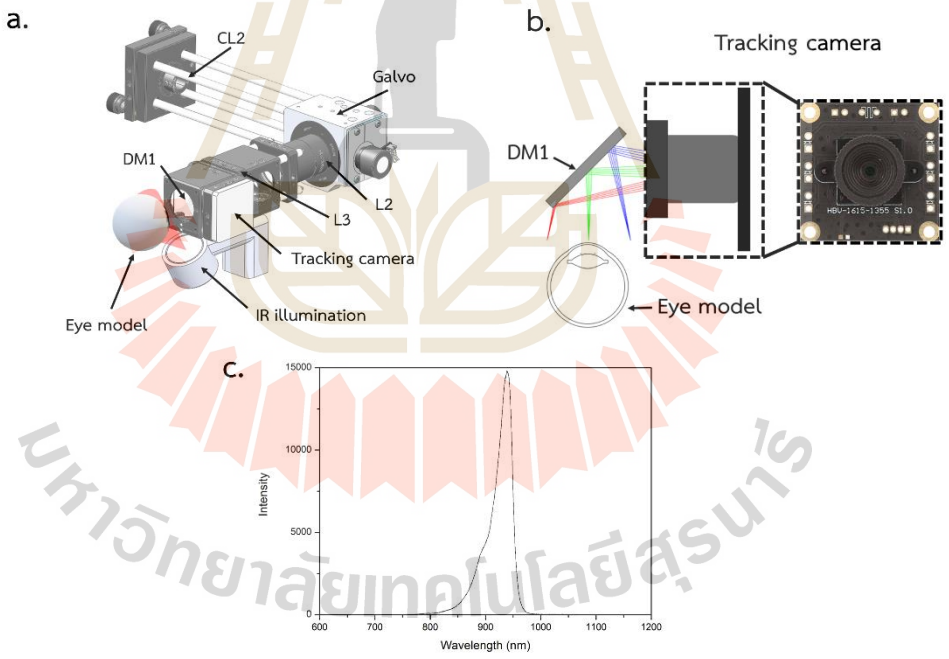

Figure 3.4 (a.) Pupil tracking system is a part of sample arm. There was an Off-axis IR Illumination at the bottom to illuminate the pupil. (b.) Optical design of the pupil tracking system, using a dichroic mirror (DM1) to reflect light from the eye to the tracking camera. (c.) Spectrum of the IR Illumination.

The optical resolution of the pupil tracking camera was calculated by first converting the length of the pupil image from pixel units to microns. Subsequently, the resolution target at group 0 element 1 (USAF 1951, Thorlabs, USA) was captured by a tracking camera to determine the number of pixels in 1 line pair **Figure 3.5**. The optical resolution was then calculated from the Full Width at Half Maximum (FWHM) of the edge peak, which is a derivative of the intensity of the line drawn through the edge of the black square in the resolution target as shown in **Figure 3.6**.

a.

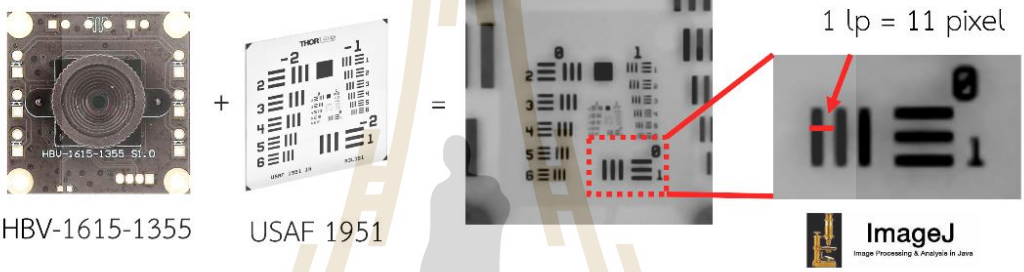

b.

Element	Group Number									
	-2	-1	0	1	2	3	4	5	6	7
1	0.250	0.500	1.00	2.00	4.00	8.00	16.00	32.00	64.00	128.00
2	0.280	0.561	1.12	2.24	4.49	8.98	17.95	36.0	71.8	144.0
3	0.315	0.630	1.26	2.52	5.04	10.10	20.16	40.3	80.6	161.0
4	0.353	0.707	1.41	2.83	5.66	11.30	22.62	45.3	90.5	181.0
5	0.397	0.793	1.59	3.17	6.35	12.70	25.39	50.8	102.0	203.0
6	0.445	0.891	1.78	3.56	7.13	14.30	28.50	57.0	114.0	228.0

Values are in lp/mm.

Figure 3.5 Demonstrates the conversion of pixel units to micron units for the pupil tracking camera by capturing the resolution target (a) and comparing it to the lookup table at group 0, element 1 (b).

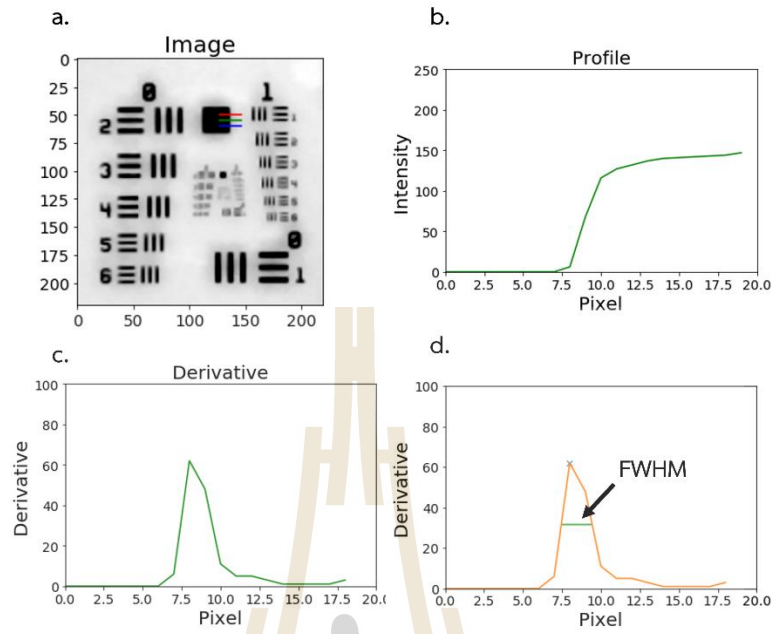

Figure 3.6 (a.) Three lines were drawn through the edge of the black square. (b.) The intensity profile of the three lines was plotted. (c.) The edge position was determined from the peak of the derivative of the intensity profile. (d.) The Full Width at Half Maximum (FWHM) of the derivative graph represents the optical resolution of the tracking camera.

To implement the pupil detection algorithm for the pupil tracker illustrated in **Figure 3.7**(a.), we employed Python programming. The process was initiated by activating the camera. Subsequently, a selection was made from a range of tracking methods, encompassing six distinct algorithms for comparison. Following this, the pupil tracking process was executed to pinpoint both the pupil's center and edge. Ultimately, these coordinates were mapped onto the camera capture, presenting the pupil in real-time as shown in **Figure 3.7**(b.).

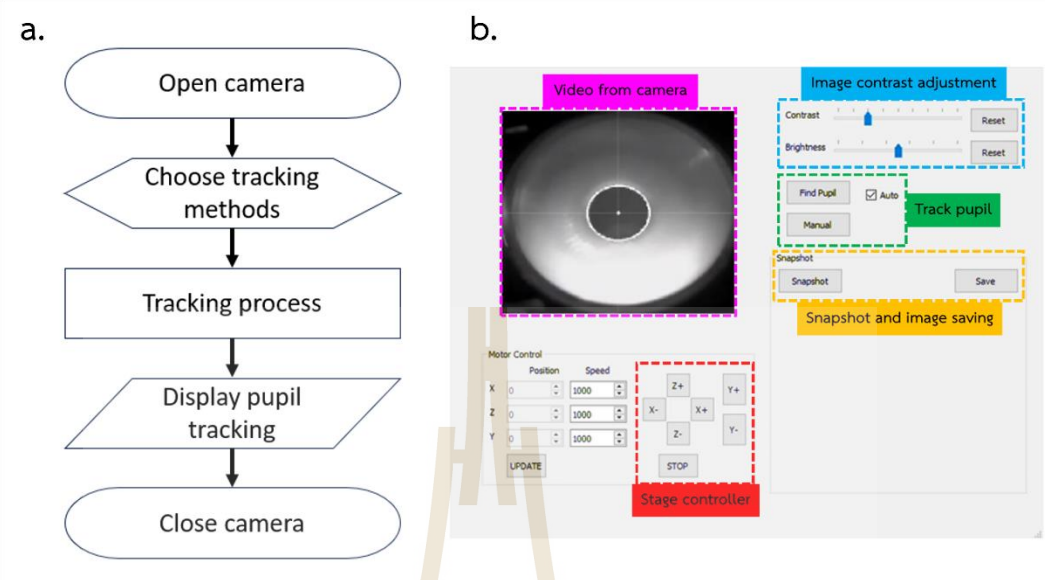

Figure 3.7 (a.) Flowchart illustrating the Pupil Tracker. (b.) Interface of the Eye Tracker, including camera video, image contrast adjustment, snapshot and image saving, pupil detection button, and stage controller.

In **Figure 3.8** shows an example of a method of the pupil tracking algorithm based-on Blob detection as following steps: An eye model's image as capture by a webcam camera (**Figure 3.8**(a.)). A raw image was blurred by using the Gaussian function for a noise reduction (**Figure 3.8**(b.)). To separate a pupil from an iris, the threshold was used to the blur image (**Figure 3.8**(c.)). After that, the Canny edge detection was used for edge fitting of a threshold image **Figure 3.8**(d.). Finally, a pupil's center was determined by using Blob detection (**Figure 3.8**(e.)).

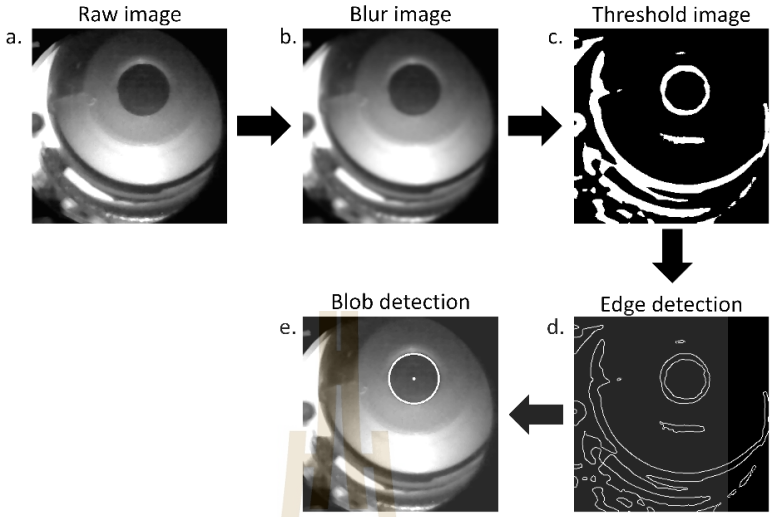

Figure 3.8 Procedure for Pupil Tracking System Using Blob Detection: (a.) Input a raw image of the pupil from a tracking camera. (b.) Apply a Gaussian function to blur the image for noise reduction. (c.) Threshold the image to separate the pupil area from the iris. (d.) Perform edge detection using a Canny filter. (e.) Utilize Blob detection to locate the center of the pupil.

3.4 Comparison of tracking algorithm

The eye phantom was used for measurement of OCT retina image quality. We used an eye phantom from Modell-Augen Manufaktur as shown in **Figure 3.9** (Lankenau, Eva. (2022, April 3). Modell-Augen Manufaktur. https://www.modell-augen-manufaktur.de/). As for the specifications of the eye model, the retina had an approximate radius of 15 mm. The posterior segment included replicas of the retinal layers, the macula, the optic nerve, and a red vessel structure in the uppermost retina layer. The posterior segment (**Figure 3.9**(b.)) continued to employ Modell-Augen Manufaktur's, while the lens on the anterior segment was replaced with an achromatic doublet lens (AC127-019-B-ML, Thorlabs, Inc.) held in place by a 3D-printed holder, as depicted in **Figure 3.9**(a.).

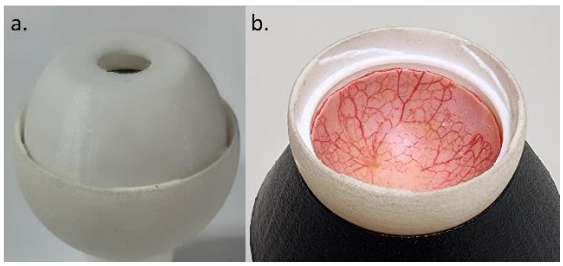

Figure 3.9 An eye phantom includes an anterior segment (a.) and posterior segment (b.).

3.4.1 Accuracy calculation

To attain precise alignment of the OCT beam within the pupil, the accuracy of pupil tracking was evaluated and compared. If the accuracy of pupil tracking was insufficient, correct alignment of the OCT beam with the pupil would not be achieved. The accuracy value is utilized as an indicator of the error in the distance between the labeled and tracked center of the pupil. The calculations for accuracy consist of four steps, as illustrated in **Figure 3.10**.

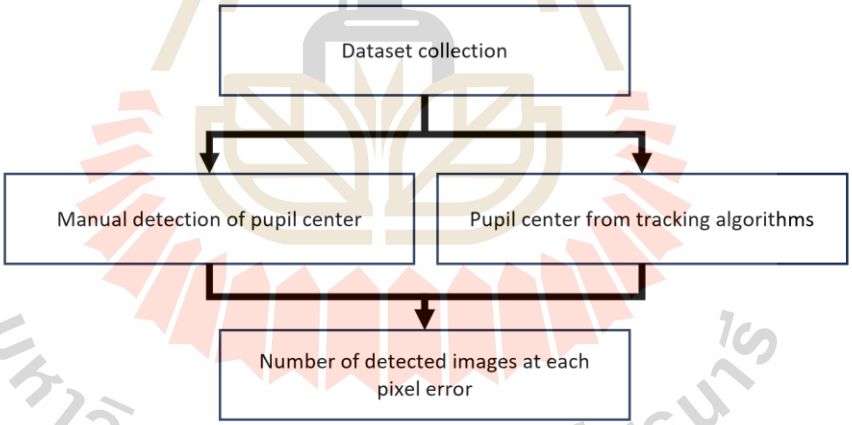

Figure 3.10 Flowchart of the accuracy calculations.

The initial stage in calculating pupil tracking accuracy involves the collection of datasets. As depicted in **Figure 3.11**, the five datasets of the eye model at different pupil locations in comparison to the intersection point (OCT beam) were obtained, with 20 photographs taken for each dataset.

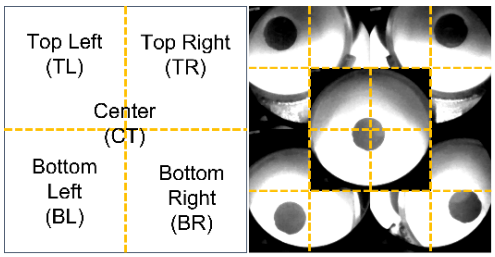

Figure 3.11 Pupil image's datasets at the different positions of pupil compared with the camera frame's center.

The steps of dataset collection were depicted in **Figure 3.12**. First, the camera was turned on. Subsequently, the pupil position was initially established within the dataset region by manual adjustment of the translation stage. Following that, the total number of captured images was set to 20. The stage was then automatically moved within the range of 0 to 40 pixels to randomize the pupil position, and an image was captured and saved. This process was repeated until 20 images were obtained. Finally, the pupil images within one dataset were collected. To gather another dataset, the initial pupil position in step two was altered within that dataset region.

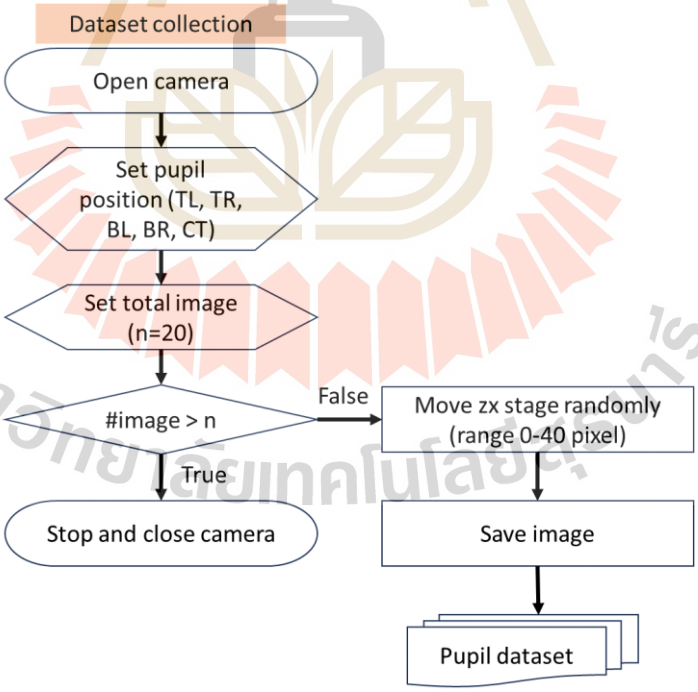

Figure 3.12 Flowchart of the dataset collection in the accuracy calculations.

In the second stage, the standard method to find the pupil's center is the centroid method, as illustrated in **Figure 3.13**. First, the pupil's image was imported

in grayscale (**Figure 3.13**(b.)). Then, the image was threshold to create a binary image (**Figure 3.13**(c.)). Next, the contours and moments of the image were calculated to locate the pupil's center. **Figure 3.13**(d.) shows the various moments of the image. Moments not corresponding to the pupil were filtered by their area. The result after applying the area filter is shown in **Figure 3.13**(e.). However, some moments still caused errors due to similar moment areas. Finally, the pupil's center was selected manually.

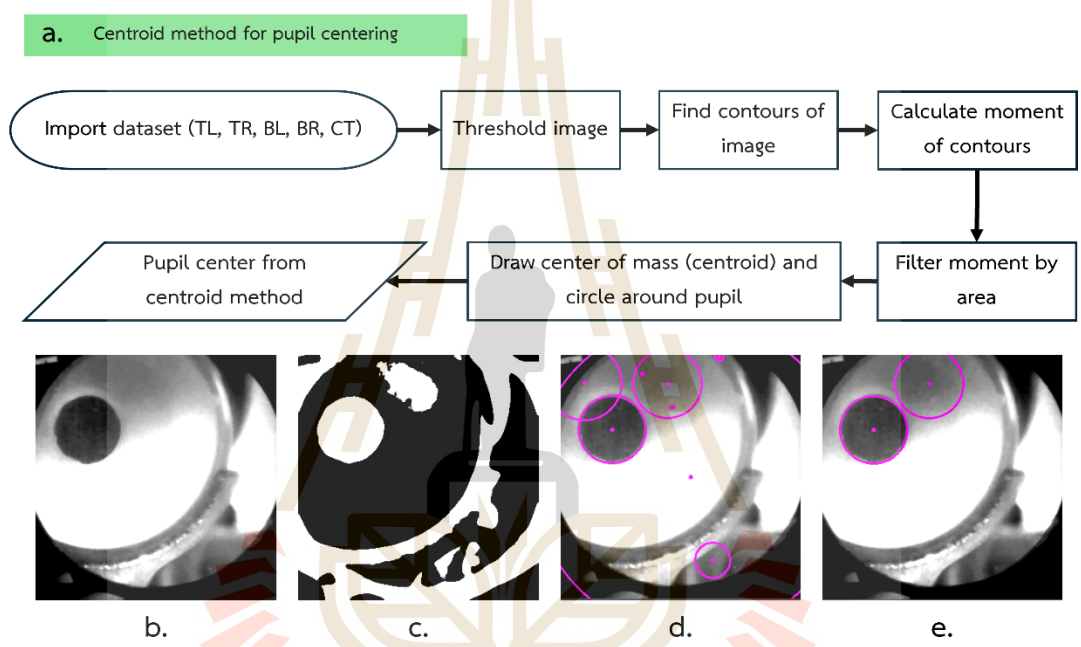

Figure 3.13 Flowchart illustrating the measurement of the pupil's center using the centroid method (a.): The pupil image (b.) was threshold (c.). The center and circumference of the pupil are then calculated from the moment of contours. (d.) and (e.) show pupil centers without and with area filtering, respectively.

We proposed the manual detection method to find pupil's center as depicted in **Figure 3.14**. The steps of manual detection method follow the following step. The pupil's center was determined for labeling using the intensity graph. By selecting a single point within the pupil area (Initial position), three horizontal lines (**Figure 3.14**(b.)) and pupil region lines (represented by black dot lines) were automatically generated. The intensity graphs of these three lines were then extracted (**Figure 3.14**(c.)), and the derivative of the intensity graphs was utilized to locate the

peaks corresponding to the pupil's edges (**Figure 3.14**(d.)). The estimated center of the pupil was determined as the midpoint between these two peaks. The average pupil centers across the three lines were considered as the final pupil center. It is important to note that **Figure 3.14** illustrates the calculation only for the x position, but in practice, the calculations are performed simultaneously for both the x- and y-axes using the same approach. The advantage of the proposed method was that it allows for the determination of the initial pupil position, reducing errors from measurements taken at locations other than the pupil.

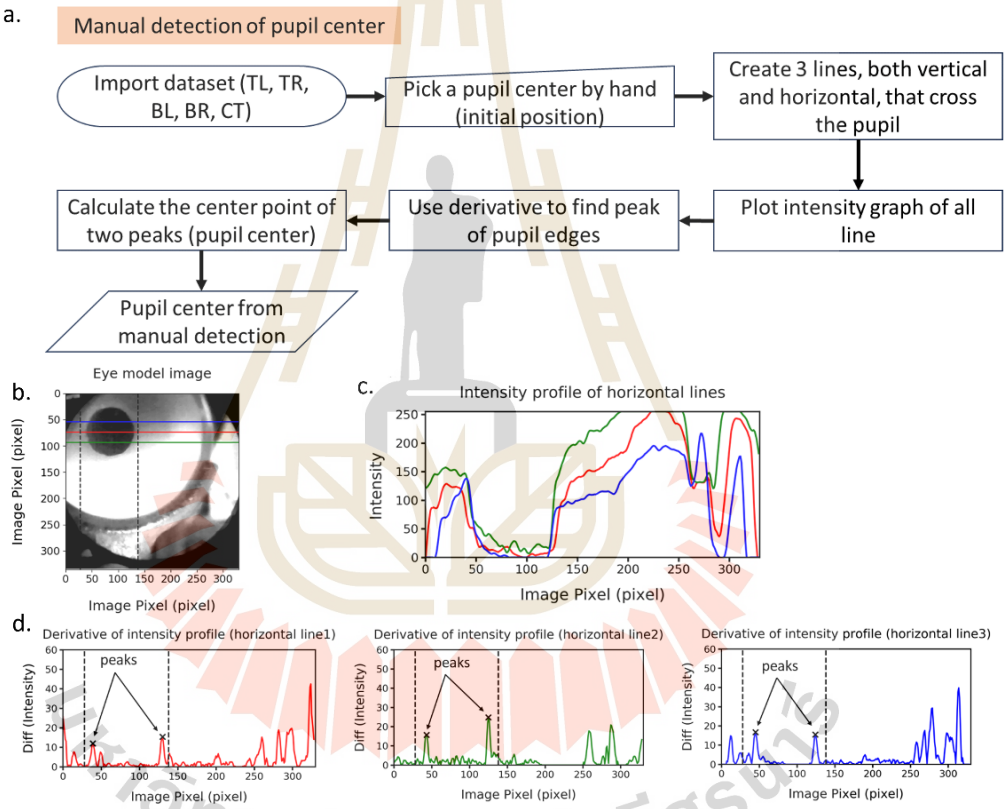

Figure 3.14 Flowchart illustrating the measurement of the pupil's center through manual detection (a). Three lines were drawn across the pupil, and the boundaries (marked by black dashes) were created automatically (b). The intensity graphs for these three lines were plotted (c). The derivatives of the intensity graphs were used to calculate the pupil's center (d).

To ensure the robustness of the calculated pupil center, we conducted experiments by varying the initial position across four different positions. The results

indicate that regardless of the initial position, the calculated pupil center consistently remained in the same location, as presented in **Table 3.1**.

Table 3.1 Comparison of the pupil center position across the different initial positions and their calculated position.

	1st time	2nd time	3rd time	4th time
Initial position	(84, 72)	(79, 74)	(86, 78)	(81, 77)
Calculated position	(84, 73)	(84, 73)	(84, 73)	(84, 73)

The next step involves locating the pupil's center using Python-based tracking algorithms, i.e. Swirski, ExCuSe, ElSe, PuRe, PuReST, and Blob. These algorithms are implemented in Python and specifically designed for pupil tracking purposes. The output obtained from these tracking algorithms, representing the estimated pupil's center, was referred to as the "pupil's center from tracking." Flowchart of this process is shown in **Figure 3.15**.

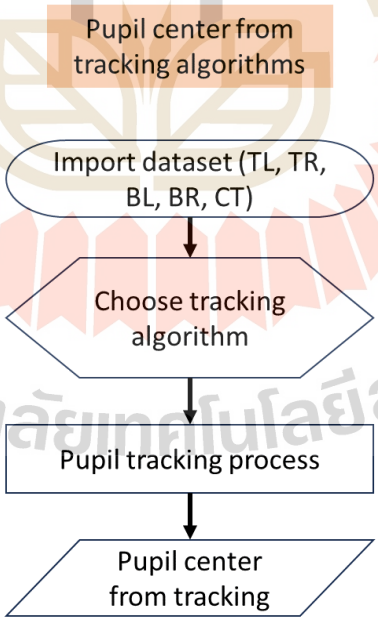

Figure 3.15 Diagram illustrating the process of tracking the pupil center using tracking algorithms.

The final step involved calculating the pixel error as shown in **Figure 3.16**, through calculating the Euclidean distance (refer to Eq. (3.1)) between the manually labeled pupil center and the center determined by each tracking method, as illustrated in **Figure 3.17**. Improved tracking algorithm accuracy is reflected in an increased number of images detected with minimal pixel error, denoting accurate tracking performance. The measure of accuracy was then determined by the area under the curve of the cumulative density function (CDF) for the number of images detected. This method of using the CDF follows the detection rate approach outlined in the literature review.

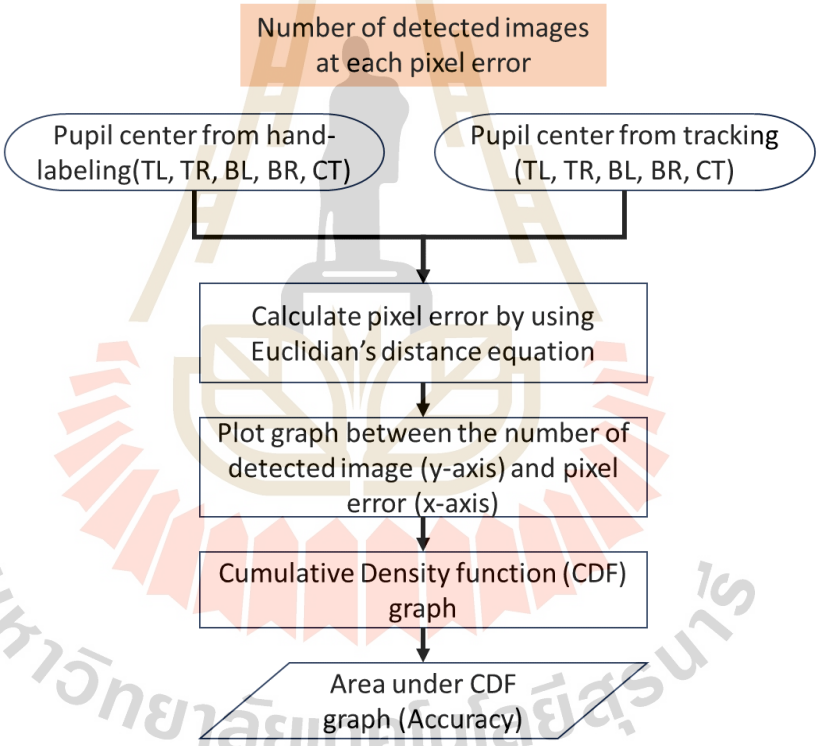

Figure 3.16 Diagram illustrating the process for computing the quantity of images detected at various levels of pixel error.

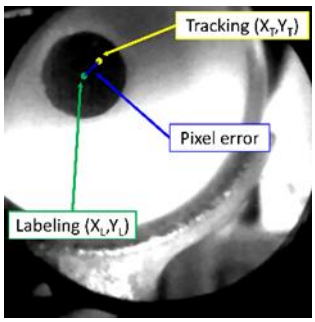

Figure 3.17 Pixel error refers to the distance measured between the labeled coordinates (x_L, y_L) and the coordinates obtained through tracking (x_T, y_T).

$$\text{Pixel error} = \sqrt{(x_T - x_L)^2 + (y_T - y_L)^2}, \tag{3.1}$$

where x_L and y_L are the position in x- and y-axis of the labeling point, and x_T and y_T are the position in x- and y-axis of the tracking point.

3.4.2 Repeatability calculation

To evaluate repeatability, a new dataset comprising 50 images of an eye model in a fixed position was collected over 100 seconds as shown in **Figure 3.18**(a.). Five datasets were created, each with distinct pupil locations. Using these datasets, the algorithms tracked the pupil under two conditions: with and without light reflection from a flashlight. Repeatability values for each algorithm were computed using the standard deviation (SD) metric as shown in **Figure 3.18**(b.). Lower SD values indicate higher repeatability, reflecting more consistent tracking performance across the dataset. This repeatability assessment enables the evaluation of algorithm capabilities in noise handling and tracking precision. Such analysis aids in selecting reliable algorithms for accurate and consistent pupil tracking, even in challenging imaging conditions.

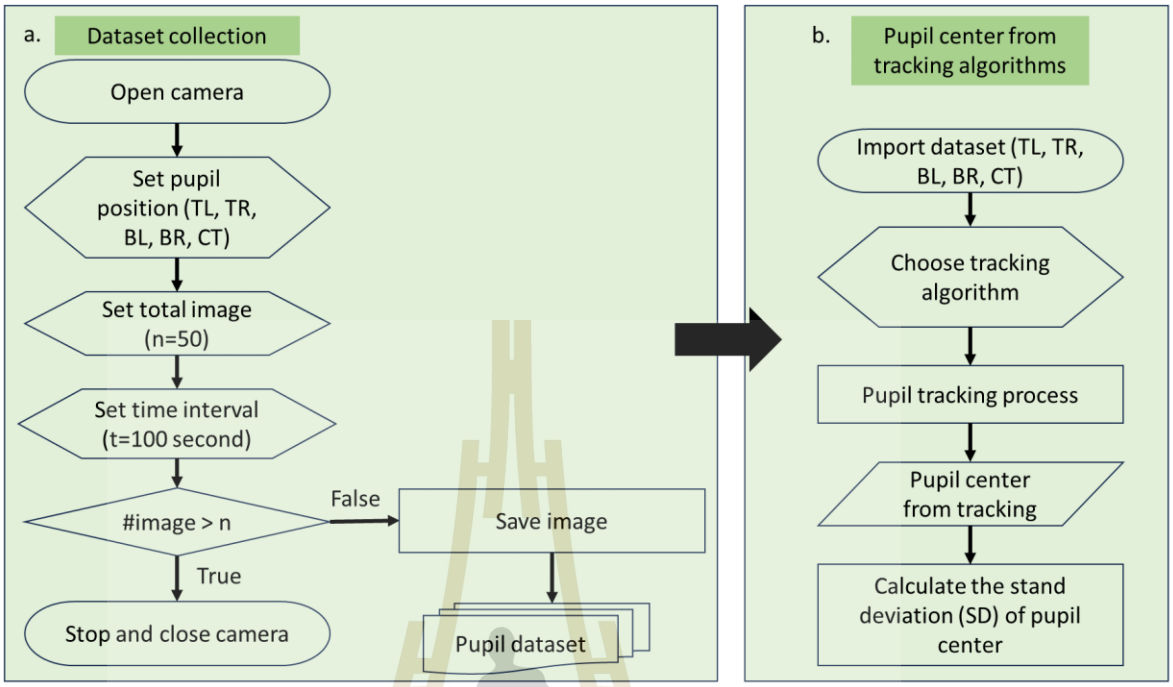

Figure 3.18 Flowchart of the calculation of the repeatability.

3.4.3 Run-time calculation

The run-time value represents the duration it takes from the start of the tracking process until obtaining the data for the pupil's center. Due to the limitation of our imaging speed, which is approximately 60 frames per second, each image acquisition takes around 16 milliseconds. Therefore, if the pupil tracking algorithm has a high run-time value (slow tracking), it can result in blurred OCT images because eye movements cannot be effectively corrected in a timely manner. To ensure real-time tracking and avoid image blurring, it is important to select an algorithm with the lowest run-time value for our tracking system. As shown in **Figure 3.19**, the run-time values were measured repeatedly, with 10 iterations performed. The run-time value of each tracking algorithm is then expressed using the average value, providing an indication of the algorithm's efficiency in terms of processing speed. By considering the run-time values of different tracking algorithms, we can identify the algorithm that offers the most suitable performance for our tracking system. Selecting an algorithm with a lower average run-time value ensures that the pupil tracking process is swift and responsive, allowing for effective correction of eye movements and enabling clear OCT image acquisition.

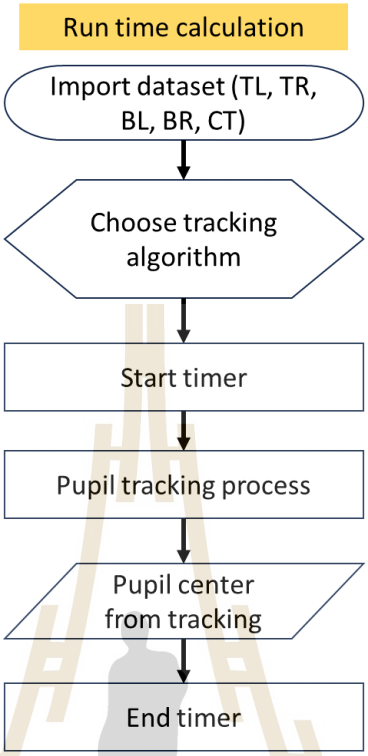

Figure 3.19 Flowchart of the run-time calculation.

3.4.4 Optimization of 3-axis stage

After selecting the optimal retina scanner algorithm, we attempted to link the 3-axis stage to shift the OCT beam to the pupil center. The translation stage is controlled by inputting the velocity value in the x-axis (v_x) and the y-axis (v_y), which is dependent on the distance between the center point of the OCT beam (which is also the center point of the camera frame) and the center point of the pupil, as illustrated in **Figure 3.20**. In Eq. (3.2) and Eq. (3.3) describe the velocity equations for the translation stage. We observed damped motion caused by an incorrect gain value. To overcome this issue, we evaluated the stage's feedback gain values in order to maximize the 3-axis stage performance. In this experiment, the center of the pupil was initially positioned at different distances from the camera's center: specifically, 60, 50, 40, 30, 20, and 10 pixels. The tracking algorithm was then utilized to track the pupil and send the data to move the motor's stage until the OCT beam was aligned with the pupil's center. Finally, at each tracking step, graphs of the distance between the pupil's center and the camera frame's center were compared.

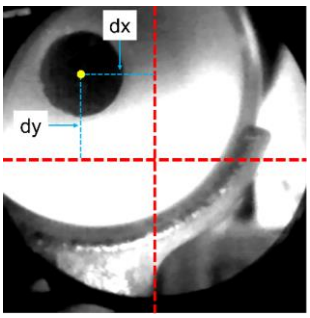

Figure 3.20 The distance between pupil's center and camera frame's center (OCT beam) in x-axis (dx) and y-axis (dy).

$$v_x = g_x \times dx, \tag{3.2}$$

$$v_y = g_y \times dy, \tag{3.3}$$

where v_x and v_y are the velocity of the translation stage in x and y-axis, respectively. g_x and g_y are the gain value in x and y-axis, respectively. dx and dy are the distance between a pupil's center and the camera frame's center in x and y-axis, respectively.

3.4.5 Eye motion correction with pupil tracking system

After the damp motion is solved, the pupil tracking system and imaging system were used in order to compensate for eye motion in an eye model. The chinrest is moved along the vertical axis for five seconds while OCT images are being taken in order to simulate an eye motion (**Figure 3.21**(a.)). The 250 OCT images in the same scanning were obtained as shown in **Figure 3.21**(b.). Finally, the intensity of OCT images was evaluated between non-tracking and tracking eye movements.

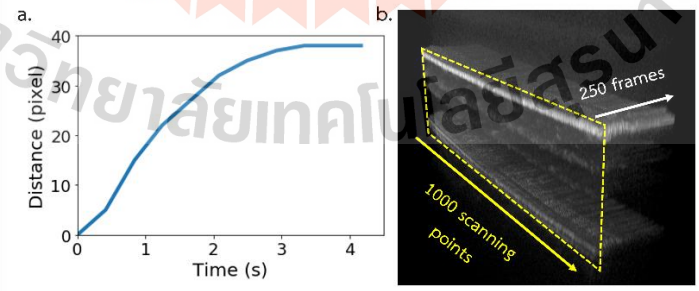

Figure 3.21 (a.) The distance between pupil's center and camera frame's center in y-axis (dy) over time with eye motion. (b.) The 3D OCT image with eye motion.

Additionally, the maximum tissue contrast index (mTCI) was calculated to represent the signal quality of OCT images. The mTCI has been formulated as a ratio of signal intensity between the foreground and the background, leveraging the histogram characteristics of the OCT images. This design allows the mTCI value to be interpreted as a measurement of signal-to-noise ratio, where a score of 1 (representing the lower limit) indicates that the signal and noise are indistinguishable, while higher values signify better image quality. Notably, there is no upper limit for the mTCI, providing the potential for achieving superior image quality in OCT scans (Huang et al., 2012).

CHAPTER IV

RESULTS AND DISCUSSIONS

4.1 Specification of OCT retina scanner

The axial resolution (ΔZ) of the OCT retina imaging from the theory can calculate follow Eq. (4.1). As shown in **Figure 4.1**, the laser source spectrum was detected by the commercial spectrometer (HR4000, Ocean Optics, Inc., USA). The full width at half maximum (FWHM) of the laser source's spectrum was 52.5 nm. The central wavelength (λ_0) was 880 nm. So, the axial resolution from theory was about 6.5 μm.

$$\Delta Z = \frac{2\ln(2)}{\pi} \cdot \frac{{\lambda_0}^2}{\Delta\lambda} \tag{4.1}$$

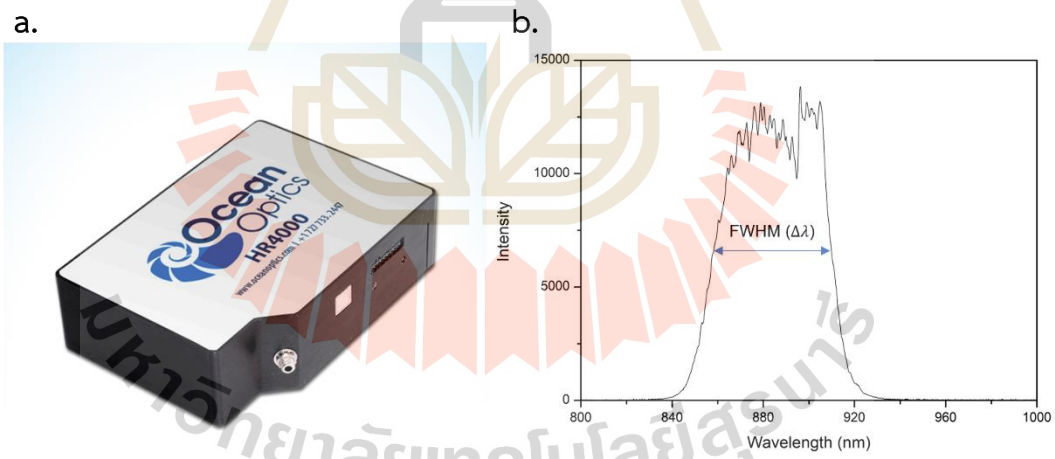

Figure 4.1 (a.) The commercial spectrometer (Ocean Optics). (b.) The source spectrum with wavelength 830-930 nm. Central wavelength was 880 nm. Bandwidth was 100 nm. FWHM was 52.5 nm.

The experimental axial resolution was measured by the FWHM of the axial point spread function (PSF), resulting from the Fourier transformation of the spectral interference signal as shown in **Figure 4.2**. The experimental axial resolution was about 7.8 μm.

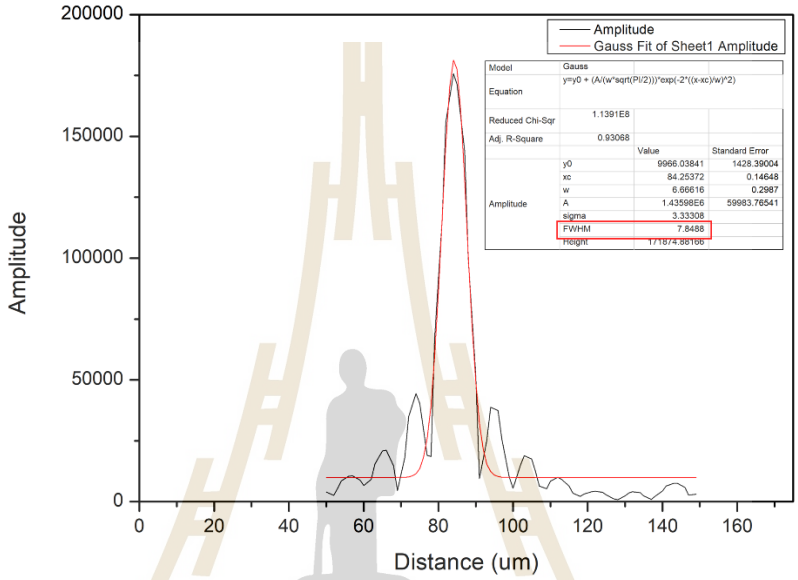

Figure 4.2 The PSF from the interference signal.

The penetration depth is the ability of the light to penetrate through the retina. In **Figure 4.3**, data each point is the peak of the PSF at the different depths by moving the reference mirror. The penetration depth was about 2.6 mm as measured by the depth location where the signal amplitude drops by 10 times from its maximum.

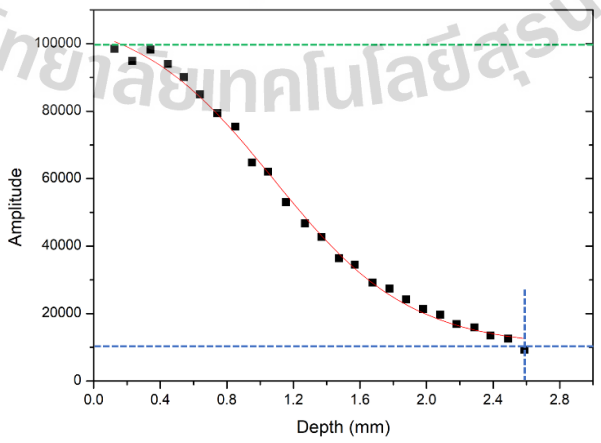

Figure 4.3 The peak amplitude of the PSF over depth.

The acquisition rate of our prototype was about 60,000 A-scans per second (based on 60 frames/second with 1000 A-scan/frame). If compared with **Table 2.1**, our prototype is similar to the Nidek RS 3000.

For the optical resolution of the pupil tracking camera, 1 line pair was equal to 11 pixels (measured from imageJ) and 1 line pair was equal to 1 mm (lookup table of USAF 1951). So, 1 pixel was equal to 0.09 mm or 90 microns. Then the FWHM represents the optical resolution of the pupil tracking camera. The resolution was 2.1 pixel or about 188 μm.

4.2 Accuracy calculation

To verify the accuracy of the pupil center calculation for the reference data from the proposed method (manual detection) compared to the standard method (centroid), the distance error of the pupil center between the two methods was compared, as shown in **Figure 4.4**. The maximum error was approximately 0.3 mm. Assuming the pupil size is equal to the OCT beam size (5.7 mm), a misalignment of 0.3 mm between the OCT beam and the pupil center is about 5%. The SNR of the PSF in **Figure 4.2** is about 12.37 dB (signal = 171875, noise = 9966). Therefore, the SNR with the misalignment is approximately 11.75 dB.

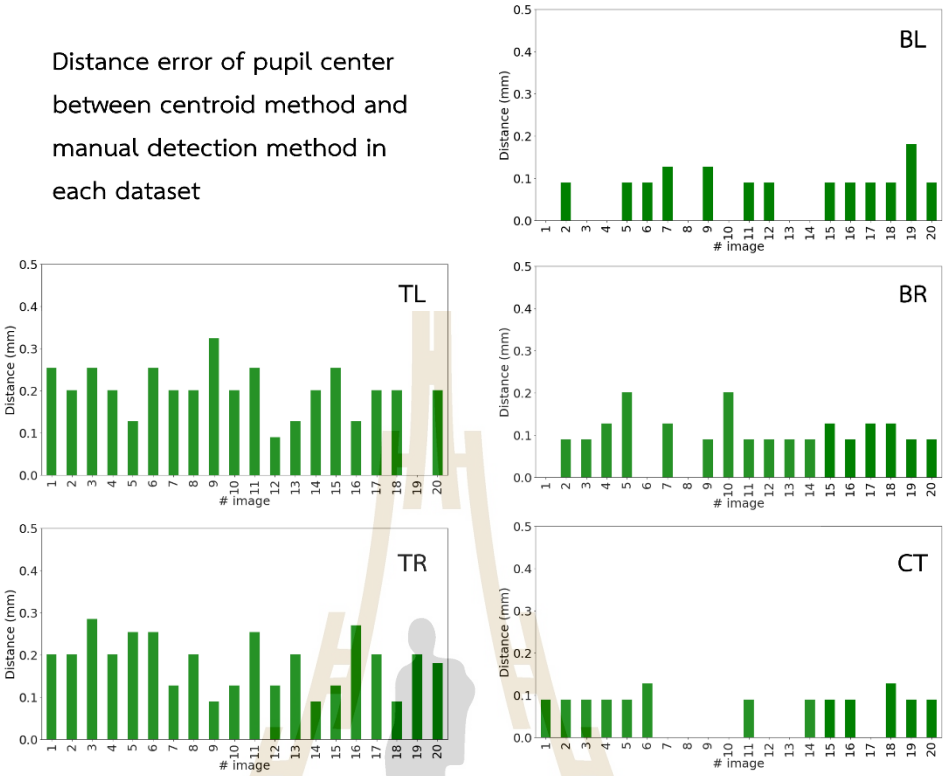

Figure 4.4 The comparison of the distance error of the pupil's center between the standard method and the proposed method in each dataset (TL, TR, BL, BR, and CT).

In **Figure 4.5**, the number of detected images by each algorithm is compared at various pixel errors. Swirski (orange) and ExCuSe (red) demonstrate lower accuracy compared to the other algorithms by looking at the large number of detected images value in the pixel error position that is more than 10 pixels. This discrepancy could be attributed to the positioning of the IR illumination, which was placed at the bottom of an eye model, resulting in stronger illumination on the pupil in the BL and BR datasets compared to the other datasets. Therefore, Blob, Else, PuRe, and PuReST yield superior results in terms of accuracy when comparing the algorithms.

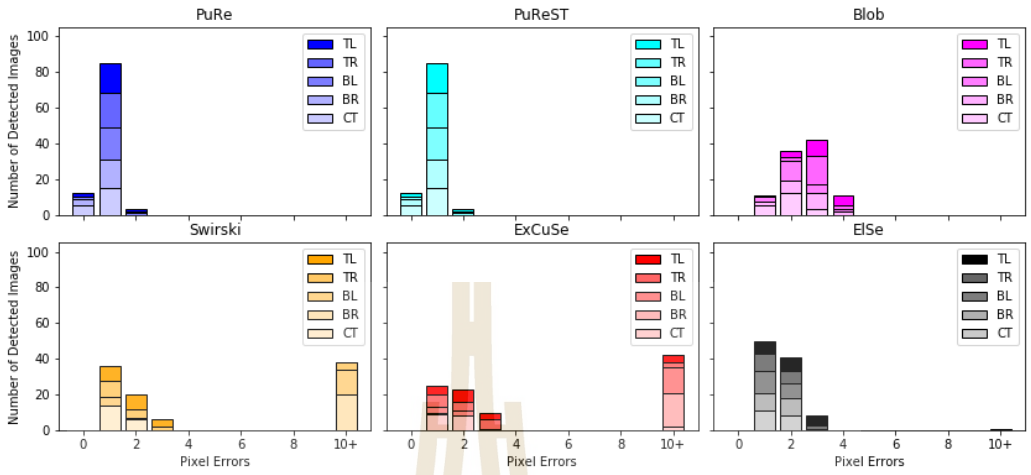

Figure 4.5 Display the cumulative count of detected images across various pixel errors for all algorithms, aggregating data from multiple datasets and representing it through shading.

Figure 4.6 displays the cumulative density of the number of detected images, enabling a comparison of the accuracy calculation for each algorithm. The area under the graph serves as a determinant of the accuracy in pupil tracking, where a larger area indicates higher accuracy. Based on the results, the PuReST algorithm exhibited the highest accuracy when compared to the other algorithms as shown in **Table 4.1**.

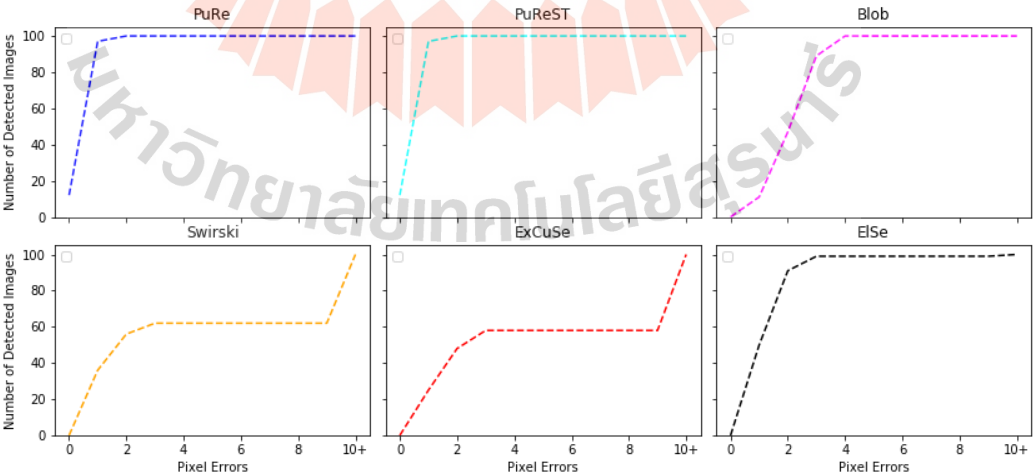

Figure 4.6 The cumulative density of the number of detected images of each algorithm.

Table 4.1 Comparison of the area under the cumulative density graph for each algorithm across the entire dataset.

Algorithms	Area under the cumulative density graph
Swirski	585.0
ExCuSe	538.5
ElSe	893.5
PuRe	977.0
PuReST	983.5
Blob	848.0

4.3 Repeatability calculation

In **Table 4.2**, the repeatability of each algorithm is compared in a dataset where visible light reflection from a flashlight is not presented. Swirski exhibits low repeatability in the BR dataset, while ExCuSe demonstrates low repeatability in both the BL and BR datasets. To assess the performance of the algorithms under reflected light conditions, visible light was introduced to the eye model, and images were collected to create a new dataset. The repeatability results for each algorithm are presented in **Table 4.3**. Interestingly, only the PuRe and Blob algorithms maintain a high level of repeatability in this scenario.

Table 4.2 The repeatability values of each algorithm in 5 datasets (no visible light reflection) were represent as the standard deviation (SD) in the x- and y-axis $(\mathbf{SD_x}, \mathbf{SD_y})$ in pixel.

Algorithms	Repeatability $(\mathbf{SD_x}, \mathbf{SD_y})$ (pixel)				
	TL-dataset	TR-dataset	BL-dataset	BR-dataset	CT-dataset
Swirski	(0, 0)	(0, 0)	(0, 0)	(13, 10)	(0, 0)
ExCuSe	(0, 0)	(0, 0)	(69, 60)	(60, 62)	(0, 0)
ElSe	(0, 0)	(0, 0)	(0, 0)	(0, 0)	(0, 0)
PuRe	(0, 0)	(0, 0)	(0, 0)	(0, 0)	(0, 0)
PuReST	(0, 0)	(0, 0)	(0, 0)	(0, 0)	(0, 0)
Blob	(0, 0)	(0, 0)	(0, 0)	(0, 0)	(0, 0)

Table 4.3 The repeatability values of each algorithm in 5 datasets (add visible light reflection) were represent as the standard deviation (SD) in the x- and y-axis $(\mathbf{SD_x}, \mathbf{SD_y})$ in pixel.

Algorithms	Repeatability $(\mathbf{SD_x}, \mathbf{SD_y})$ (pixel)				
	TL-dataset	TR-dataset	BL-dataset	BR-dataset	CT-dataset
Swirski	(1, 0)	(0, 0)	(0, 0)	(32, 21)	(0, 0)
ExCuSe	(42, 35)	(7, 4)	Not detect	(14, 13)	(0, 0)
ElSe	(34, 35)	(31, 21)	(0, 0)	(0, 1)	(0, 1)
PuRe	(0, 0)	(0, 0)	(0, 0)	(0, 0)	(0, 0)
PuReST	(0, 0)	(5, 3)	(0, 0)	(4, 4)	(0, 0)
Blob	(0, 0)	(0, 0)	(0, 0)	(0, 0)	(0, 0)

4.4 Run-time calculation

Continuing with the analysis, we provide the runtime values in **Table 4.4**. Among the algorithms, the PuReST algorithm demonstrates the fastest pupil tracking,

followed by PuRe and ExCuSe. ElSe and Blob exhibit similar runtime values, indicating comparable efficiency in their execution. However, it is noteworthy that the runtime of the Swirski algorithm displays significant fluctuations, indicating potential variability in its performance.

Table 4.4 Run-time values of each algorithm in 5 datasets.

Algorithms	Run time (ms)				
	TL-dataset	TR-dataset	BL-dataset	BR-dataset	CT-dataset
Swirski	107.3	718.6	662.9	1080.3	62.3
ExCuSe	85.3	87.1	85.0	89.3	81.8
ElSe	130.8	132.9	126.9	133.4	126.8
PuRe	71.6	72.2	64.3	68.5	67.9
PuReST	40.7	42.5	59.5	55.0	37.8
Blob	130.2	130.5	131.8	130.5	126.3

4.5 Optimization of 3-axis stage

The optimization of the stage's feedback gain values was performed using the PuReST algorithm, as depicted in **Figure 4.7**. The objective was to identify the optimal gain value that would enable the translation stage to reach a steady state in the shortest possible time. In **Figure 4.7**, the initial starting point before tracking was approximately 60 pixels. The optimal gain values obtained were 17 for the x-axis and 11 for the y-axis. These values yielded the desired outcome in terms of achieving a stable state efficiently.

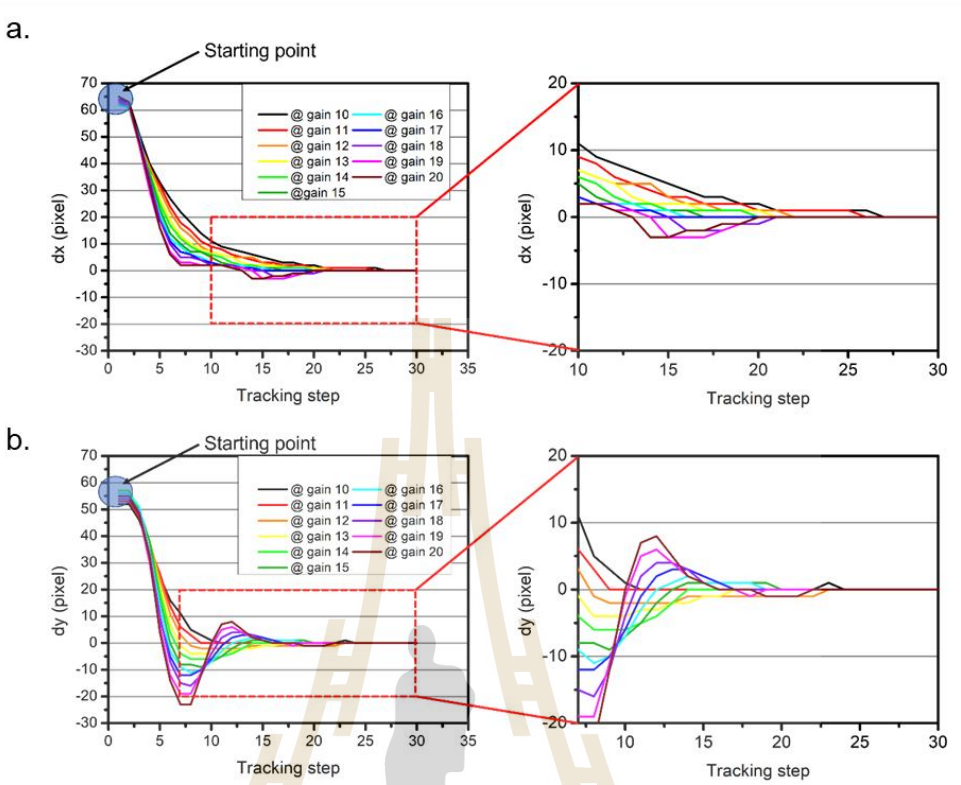

Figure 4.7 The comparison of the feedback gain values to the stage movement by using the PuReST algorithm in x-axis (a.) and y-axis (b.).

To investigate whether changing the starting point of the pupil's center affects the gain value, we examined the results presented in **Table 4.5**. It was observed that the best feedback gain value in the x-axis remained constant (averaging at 17). However, the gain value in the y-axis varied because the types of the translation stages in the x-axis and y-axis were different. By employing the gain values provided in **Table 4.5**, we observed a reduction in damp motion, as illustrated in **Figure 4.8**. The different colors in **Figure 4.8** correspond to distinct starting points before tracking, showcasing the impact of the gain values on the motion dampening effect.

Table 4.5 The optimal feedback gain values at the different starting point.

Starting point	Feedback gain	
	x-axis (g_x)	y-axis (g_y)
10	17	18
20	16	14
30	17	12
40	18	11
50	17	11
60	17	11

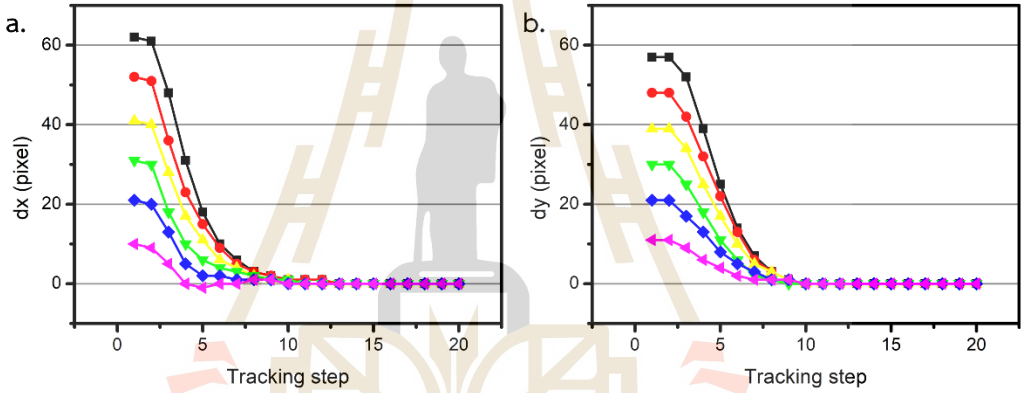

Figure 4.8 Stage movement at the different starting point which the feedback gain value of x-axis is 17 and y-axis is followed by **Table 4.5**.

4.6 Eye motion correction with pupil tracking system

Figure 4.9 provides a comparison of the 3D OCT images of the eye in motion, contrasting the non-tracking scenario (**Figure 4.9**(a.)) with the tracking scenario (**Figure 4.9**(b.)). The solid lines and dot lines correspond to images captured near the starting and ending points of the eye's motion, respectively. Furthermore, the intensity graph in **Figure 4.9**(c.) demonstrates that the intensity of the non-tracking condition (represented by the red line) and the tracking condition (represented by the green line) were initially similar. However, a notable intensity drop occurs in the non-tracking condition (red dot) towards the end, as indicated in **Figure 4.9**(d.).

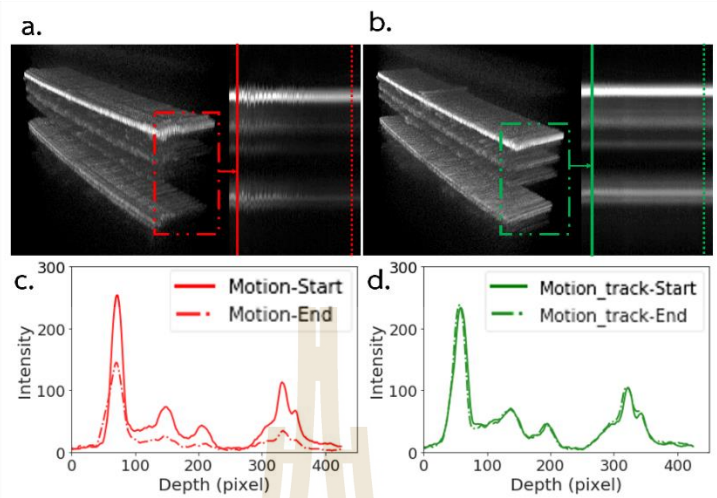

Figure 4.9 The 3D OCT image showcases an eye undergoing motion, comparing scenarios without tracking (a.) and with tracking (b.). In the intensity graphs for both the non-tracking (c.) and tracking (d.) motions, the image intensity at the onset of the eye movement is shown with solid lines. The intensity at the end of the eye movement is indicated by dotted lines.

Figure 4.10(a.) shows the cumulative density function of the image at the end of the eye motion with tracked and non-tracked motion. The experimental results are consistent with (Huang et al., 2012), indicating that OCT images with weaker signals tend to exhibit a higher number of pixels at low pixel intensities. Then, **Figure 4.10**(b.) was created with the purpose of providing a visual representation of the trend in mTCI values observed in 3D images under both tracked and non-tracked motion conditions. This graph allows us to compare the behavior of mTCI values between the two scenarios and gain insights into their respective trends. Upon analyzing the trend line of the mTCI value for tracked motion, we observe that it remains relatively stable throughout the imaging process. This consistency suggests that the tracking algorithm successfully compensates for eye motion, enabling the maintenance of signal quality and contrast in the OCT images. The stable trend line confirms the accuracy and robustness of the tracking algorithm in effectively capturing the pupil's center and correcting for motion-induced artifacts. In contrast, the trend line of the mTCI value for non-tracked motion shows a distinct and notable decrease over time. This decline in mTCI values is directly linked to the presence of uncorrected eye motion during image acquisition. As the eye moves, it introduces motion artifacts, leading to reduced

signal quality and decreased contrast in the OCT images. Consequently, the mTCI values diminish progressively, indicating a degradation in the image quality and visibility of tissue structures. By comparing these trends, we can appreciate the importance of implementing a reliable tracking algorithm in our imaging system. The ability of the tracking algorithm to maintain a stable trend line for mTCI values ensures improved image quality, enabling accurate and detailed visualization of retinal structures. This valuable information aids in diagnosing potential abnormalities and enhances the effectiveness of our OCT imaging system for various clinical applications in ophthalmology and vision research.

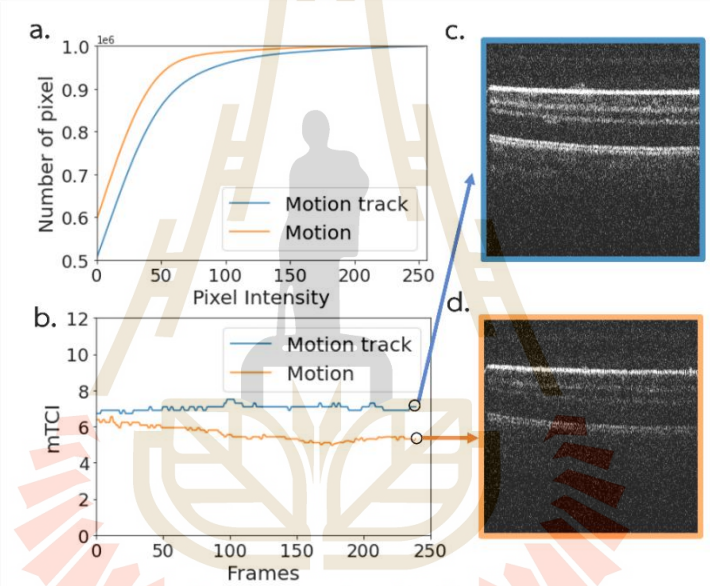

Figure 4.10 The cumulative density of histograms (a.) between the OCT image at the last frame (the end of eye motion) of tracking (c.) and non-tracking (d.) demonstrates the ability to differentiate the quality of OCT images. The mTCI values of a 3D image, separated into individual frames (b.), were compared between tracking motion (blue line) and non-tracking motion (orange line). The mTCI values at the last frame of tracking and non-tracking motion are 7.08 and 5.31, respectively.

The trend line of the mTCI values in **Figure 4.10** comes from PuReST algorithm. To determine whether the mTCI values of other algorithms remain as stable as PuReST. The mTCI value of Swirski, ExCuSe, ElSe, PuRe, and blob were calculated. As a result in **Figure 4.11**, Swirski and ExCuSe were unable to correctly detect the

center of the pupil. Meanwhile, the Blob algorithm cannot detect the center of the pupil. These made the motorized translation stage unable to move the sample arm to align the pupil. What makes these 3 algorithms unable to correctly detect the center of the pupil is due to the scan light from OCT in the pupil.

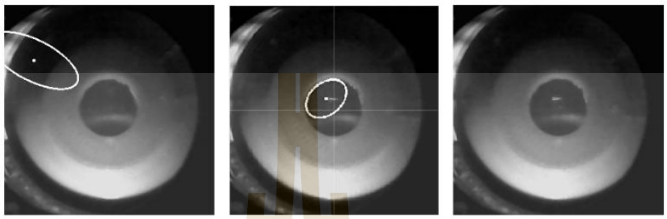

Figure 4.11 Operation of the Pupil Tracking System during the OCT scan of Swirski (a.), ExCuSe (b.), and Blob (c.).

So, there are only three algorithms (ElSe, PuRe, and PuReST) which can detect the pupil center during the OCT scan as shown in **Figure 4.12**. For the non-tracking trend line, it starts at a higher mTCI value but decreases significantly, indicating a drop in performance over time. For ElSe trend line, it maintains a relatively stable performance, with minor fluctuations, but starts to slightly decrease around frame 100. PuRe and PuReST show stable performance with minimal fluctuations, indicating consistent performance.

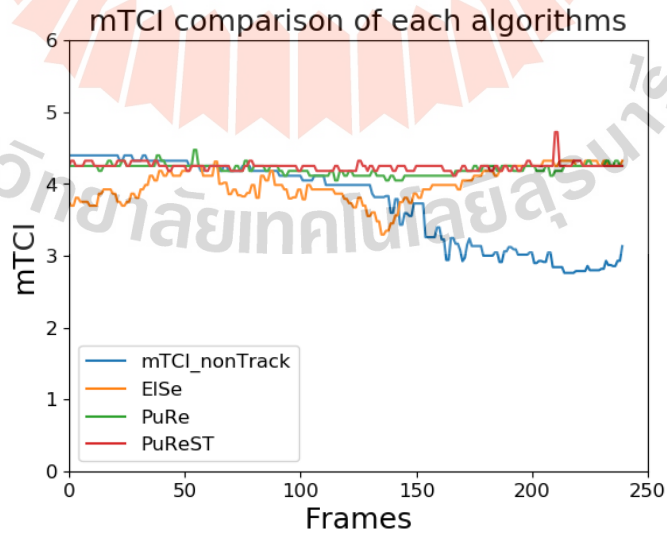

Figure 4.12 The comparison of mTCI values during the OCT imaging of the moving eye of ElSe, PuRe, and PuReST.

CHAPTER V
SUMMARY AND FUTURE WORK

5.1 Summary

First, the OCT retina scanner was developed through Michelson interferometry, employing an 880 nm near-infrared laser. Theoretical and experimental assessments yielded axial resolutions of approximately 6.5 μm and 7.8 μm, respectively. The penetration depth reached approximately 2.6 mm. Notably, our prototype achieved an acquisition rate of approximately 60,000 A-scans per second.

Second, we incorporated pupil-tracking algorithms, originally designed for AR/VR, into our custom pupil imaging system and combined it with OCT retinal imaging. We evaluated various pupil tracking algorithms (Swirski, ExCuSe, ElSe, PuRe, PuReST, and Blob) based on accuracy, repeatability, and run time. PuReST, with superior performance, was integrated into our OCT retina scanner to counteract eye movement and enhance image quality.

During this process, we identified a damp motion issue due to an inappropriate gain value. Through detailed testing, we established the optimal feedback gain values: 17 for the x-axis and a value from Table 4.5 for the y-axis. With these corrections, our system effectively compensated for eye motion in an eye model. Our evaluations showed mTCI values of 7.08 and 5.31 for tracked and non-tracked motions at the final frame, respectively. The mTCI trend for tracked motion was consistent, signifying stable image quality. In contrast, non-tracked motion exhibited a decreasing mTCI trend, emphasizing the impact of eye movement. In practical use, the Swirski, ExCuSe, and Blob do not work because they cannot detect the pupil center during the OCT imaging due to the light from OCT scan at the pupil. Although the ElSe can detect the pupil center, the mTCI value is not stable enough to be used to track the pupil. The

algorithm that can be used to track pupils while OCT imaging is PuRe and PuReST, based on the stable trend line of mTCI value.

In future work, we will redesign the sample arm for friendly use by increasing the working distance between the sample arm and the patient's eye. For the OCT imaging program, we will change from LabVIEW to Python to be convenient for commercial build.

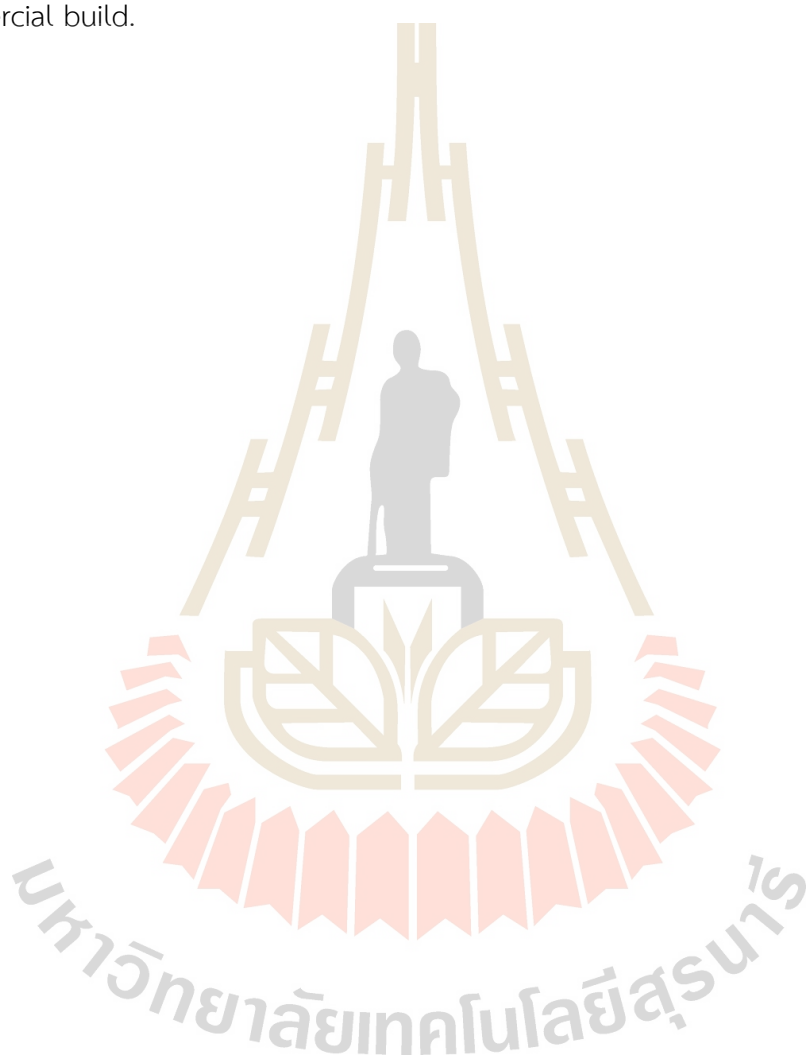

REFERENCES

REFERENCES

Bille, J. F. (2019). High resolution imaging in microscopy and ophthalmology: new frontiers in biomedical optics.

Canny, J. (1986). A computational approach to edge detection. *IEEE Transactions on pattern analysis and machine intelligence*(6), 679-698.

Carrasco-Zevallos, O., Nankivil, D., Keller, B., Viehland, C., Lujan, B. J., and Izatt, J. A. (2015). Pupil tracking optical coherence tomography for precise control of pupil entry position. *Biomedical Optics Express*, *6*(9), 3405-3419. https://www.ncbi.nlm.nih.gov/pmc/articles/PMC4574666/pdf/3405.pdf

Casas, J. P., and Chandrasekaran, C. (2019). OpenEyeTrack-a high speed multi-threaded eye tracker for head-fixed applications. *Journal of Open Source Software*, *4*(42), 1631.

Chopra, R., Wagner, S. K., and Keane, P. A. (2021). Optical coherence tomography in the 2020s—outside the eye clinic. *Eye*, *35*(1), 236-243. https://www.nature.com/articles/s41433-020-01263-6.pdf

Drexler, W., and Fujimoto, J. G. (2008). *Optical coherence tomography: technology and applications*. Springer Science & Business Media.

Fercher, A. F., Hitzenberger, C. K., Kamp, G., and El-Zaiat, S. Y. (1995). Measurement of intraocular distances by backscattering spectral interferometry. *Optics communications*, *117*(1-2), 43-48.

Fischler, M. A., and Bolles, R. C. (1981). Random sample consensus: a paradigm for model fitting with applications to image analysis and automated cartography. *Communications of the ACM*, *24*(6), 381-395.

Fouras, A., Kitchen, M. J., Dubsky, S., Lewis, R., Hooper, S. B., and Hourigan, K. (2009). The past, present, and future of x-ray technology for in vivo imaging of function and form. *Journal of Applied Physics*, *105*(10), 102009.

Fuhl, W., Kübler, T., Sippel, K., Rosenstiel, W., and Kasneci, E. (2015). Excuse: Robust pupil detection in real-world scenarios. International conference on computer analysis of images and patterns,

Fuhl, W., Santini, T. C., Kübler, T., and Kasneci, E. (2016). Else: Ellipse selection for robust pupil detection in real-world environments. Proceedings of the Ninth Biennial ACM Symposium on Eye Tracking Research & Applications,

Fuhl, W., Tonsen, M., Bulling, A., and Kasneci, E. (2016). Pupil detection for head-mounted eye tracking in the wild: an evaluation of the state of the art. *Machine Vision and Applications*, *27*(8), 1275-1288.

Fukuma, Y., Tokuda, K., Taiki, A., Kubota, A., and Ono, Y. (2016). Ophthalmologic apparatus. In: Google Patents.

Gibson, E. A., Masihzadeh, O., Lei, T. C., Ammar, D. A., and Kahook, M. Y. (2011). Multiphoton microscopy for ophthalmic imaging. *Journal of ophthalmology*, 2011.

Hogan, J. N. (2018). Head-mounted optical coherence tomography. In: Google Patents.

Huang, D., Swanson, E. A., Lin, C. P., Schuman, J. S., Stinson, W. G., Chang, W.,...Puliafito, C. A. (1991). Optical coherence tomography. *science*, *254*(5035), 1178-1181. https://www.ncbi.nlm.nih.gov/pmc/articles/PMC4638169/pdf/nihms692532.pdf

Huang, Y., Gangaputra, S., Lee, K. E., Narkar, A. R., Klein, R., Klein, B. E.,...Danis, R. P. (2012). Signal quality assessment of retinal optical coherence tomography images. *Investigative ophthalmology & visual science*, *53*(4), 2133-2141.

Keeler, C. R. (2002). The ophthalmoscope in the lifetime of Hermann von Helmholtz. *Archives of Ophthalmology*, *120*(2), 194-201. https://jamanetwork.com/journals/jamaophthalmology/articlepdf/269625/esa10027.pdf

Kiernan, D. F., Mieler, W. F., and Hariprasad, S. M. (2010). Spectral-domain optical coherence tomography: a comparison of modern high-resolution retinal imaging systems. *American journal of ophthalmology*, *149*(1), 18-31. e12.

Mohammed, G. J., Hong, B. R., and Jarjes, A. A. (2010). Accurate pupil features extraction based on new projection function. *Computing and Informatics*, *29*(4), 663-680.

Morimoto, C. H., Koons, D., Amir, A., and Flickner, M. (2000). Pupil detection and tracking using multiple light sources. *Image and vision computing*, *18*(4), 331-335.

Novotny, H. R., and Alvis, D. L. (1961). A method of photographing fluorescence in circulating blood in the human retina. *Circulation*, *24*(1), 82-86.

Organisciak, D. T., and Vaughan, D. K. (2010). Retinal light damage: mechanisms and protection. *Progress in retinal and eye research*, *29*(2), 113-134. https://www.ncbi.nlm.nih.gov/pmc/articles/PMC2831109/pdf/nihms165393.pdf

Oshitari, T., Hanawa, K., and Adachi-Usami, E. (2009). Changes of macular and RNFL thicknesses measured by Stratus OCT in patients with early stage diabetes. *Eye*, *23*(4), 884-889. https://www.nature.com/articles/eye2008119.pdf

Pearce, J. M. (2009). The ophthalmoscope: Helmholtz's augenspiegel. *European neurology*, *61*(4), 244-249.

Puliafito, C. A., Hee, M. R., Lin, C. P., Reichel, E., Schuman, J. S., Duker, J. S.,...Fujimoto, J. G. (1995). Imaging of macular diseases with optical coherence tomography. *Ophthalmology*, *102*(2), 217-229. https://www.aaojournal.org/article/S0161-6420(95)31032-9/pdf

Ryan, S. J., Hinton, D. R., Sadda, S. R., and Schachat, A. P. (2012). *Retina* (Vol. 1). Elsevier Health Sciences.

Santini, T., Fuhl, W., and Kasneci, E. (2018a). PuRe: Robust pupil detection for real-time pervasive eye tracking. *Computer Vision and Image Understanding*, *170*, 40-50. https://doi.org/https://doi.org/10.1016/j.cviu.2018.02.002

Santini, T., Fuhl, W., and Kasneci, E. (2018b). PuReST: Robust pupil tracking for real-time pervasive eye tracking. Proceedings of the 2018 ACM symposium on eye tracking research & applications,

Sheehy, C. K., Yang, Q., Arathorn, D. W., Tiruveedhula, P., de Boer, J. F., and Roorda, A. (2012). High-speed, image-based eye tracking with a scanning laser ophthalmoscope. *Biomedical Optics Express*, *3*(10), 2611-2622. https://www.ncbi.nlm.nih.gov/pmc/articles/PMC3469984/pdf/2611.pdf

Swanson, E. A., Izatt, J. A., Hee, M. R., Huang, D., Lin, C., Schuman, J.,...Fujimoto, J. G. (1993). In vivo retinal imaging by optical coherence tomography. *Optics letters*, *18*(21), 1864-1866.

Świrski, L., Bulling, A., and Dodgson, N. (2012). Robust real-time pupil tracking in highly off-axis images. Proceedings of the symposium on eye tracking research and applications,

Vienola, K. V., Braaf, B., Sheehy, C. K., Yang, Q., Tiruveedhula, P., Arathorn, D. W.,...Roorda, A. (2012). Real-time eye motion compensation for OCT imaging with tracking SLO. *Biomedical Optics Express*, *3*(11), 2950-2963. https://www.ncbi.nlm.nih.gov/pmc/articles/PMC3493227/pdf/2950.pdf

Virgili, G., Menchini, F., Casazza, G., Hogg, R., Das, R. R., Wang, X., and Michelessi, M. (2015). Optical coherence tomography (OCT) for detection of macular oedema in patients with diabetic retinopathy. *Cochrane Database of Systematic Reviews*(1).

Waheed, N. K., Moult, E. M., Fujimoto, J. G., and Rosenfeld, P. J. (2016). Optical coherence tomography angiography of dry age-related macular degeneration. *OCT Angiography in Retinal and Macular Diseases*, *56*, 91-100.

Wang, L. V., and Wu, H.-i. (2012). *Biomedical optics: principles and imaging*. John Wiley & Sons.

Wei, J., Jing, C., Huang, T., and Stanescu, D. (2016). Automatic alignment of an imager. In: Google Patents.

Wojtkowski, M., Leitgeb, R., Kowalczyk, A., Bajraszewski, T., and Fercher, A. F. (2002). In vivo human retinal imaging by Fourier domain optical coherence tomography. *Journal of biomedical optics*, *7*(3), 457-463.

Yasin Alibhai, A., Or, C., and Witkin, A. J. (2018). Swept source optical coherence tomography: a review. *Current Ophthalmology Reports*, *6*, 7-16.

Zhu, Z., and Ji, Q. (2005). Robust real-time eye detection and tracking under variable lighting conditions and various face orientations. *Computer Vision and Image Understanding*, *98*(1), 124-154.

APPENDICES

APPENDIX A

LABVIEW 2017 PROGRAMING OF THE RETINAL IMAGING :

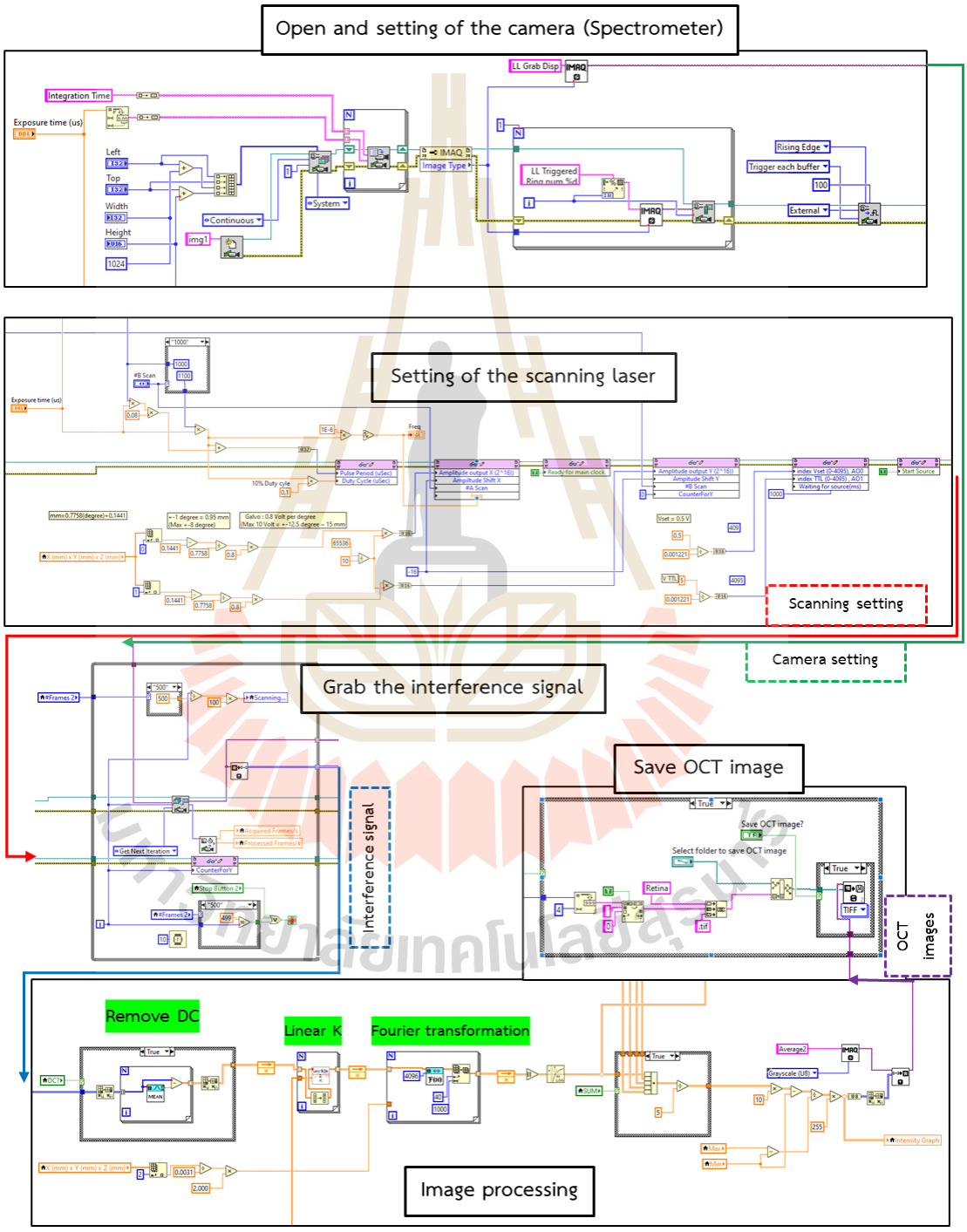

APPENDIX B

PYTHON PROGRAMING OF THE PUPIL TRACKING :

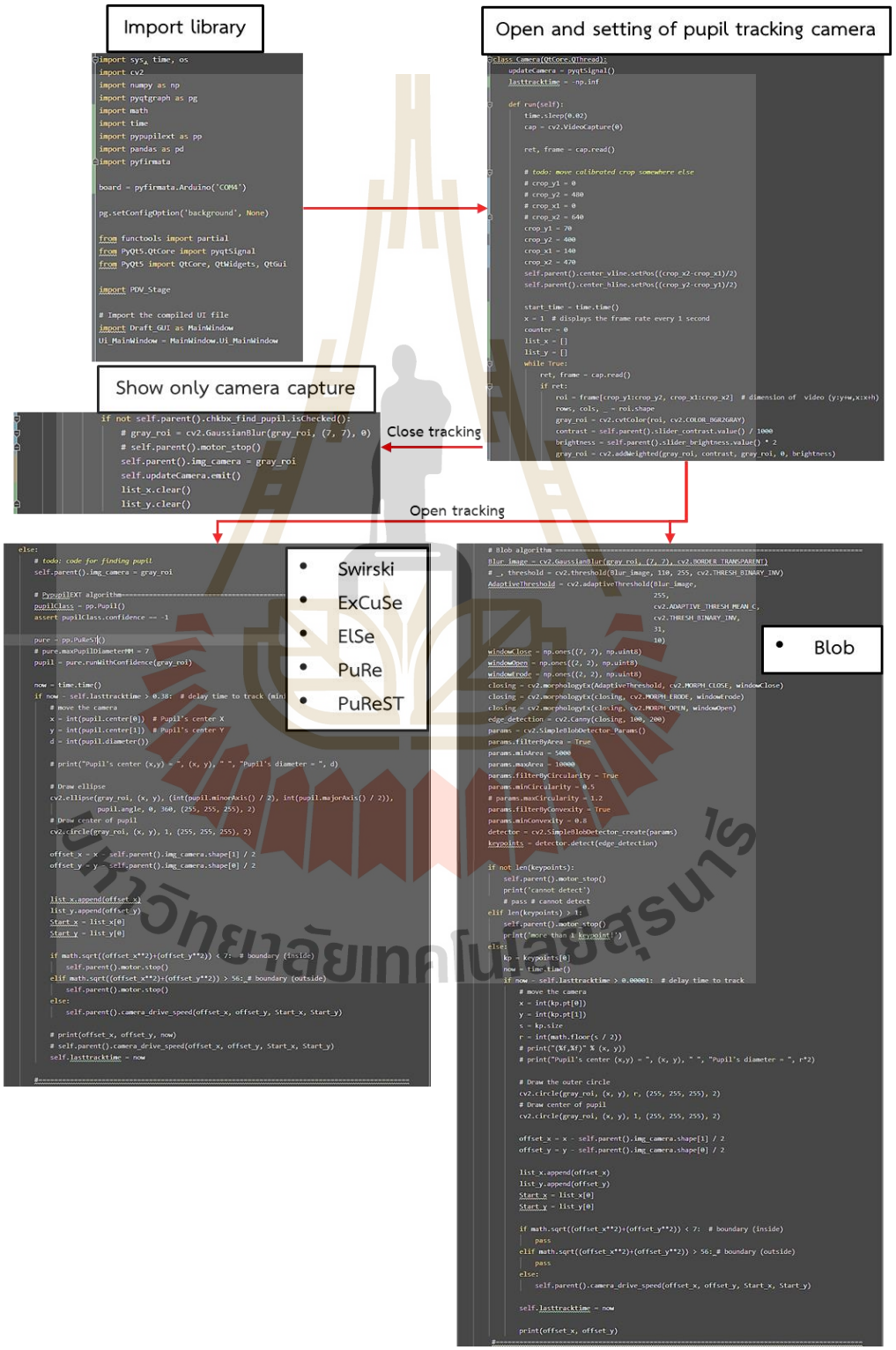

CURRICULUM VITAE

Name : Mr.Thanapol Tuntrakul

Telephone : +668 4828 6252

E-mail : thanapol.aof@gmail.com

Scholarships : Development and Promotions of Science and Technology Talents Project (DPST)

Education

2017-2024 : Ph.D. in Applied Physics
Suranaree University of Technology, Thailand

2013-2016 : Bachelor's degree in Physics
Suranaree University of Technology, Thailand

2010-2012 : Scientific Secondary School
Ratchasima Witthayalai School, Thailand

Awards

02/2024 Invention Award Fiscal year 2024
: Prototype of a Three-dimensional Retina Scanner
National Research Council of Thailand (NRCT), Thailand

Work experience

11/2022 QTFT's Workshop on Introduction to Optimization
: Attended the QTFT's Workshop
QUANTUM TECHNOLOGY FOUNDATION (THAILAND)

06/2022 The 17TH Siam Physics Congress 2022 "Carbon Neutrality"
: Poster Presentation on titled "Optical Coherence Tomography Retina Scanner"
Suranaree University of Technology, Thailand

07/2015 International Young Physicist Tournament
: Support Thai audients in competition room
Suranaree University of Technology, Thailand